

Oxidation reactions with inorganic materials:  
synthesis of methacrylic acid by supported gold  
catalysts and formation of vinylene carbonate  
by cathode active materials of lithium-ion  
batteries

邱, 逸飛

<https://hdl.handle.net/2324/6787410>

---

出版情報 : Kyushu University, 2022, 博士 (理学) , 課程博士  
バージョン :  
権利関係 :



KYUSHU UNIVERSITY  
GRADUATE SCHOOL OF SCIENCE

A THESIS SUBMITTED FOR THE DEGREE OF  
DOCTOR OF PHILOSOPHY

**Oxidation reactions with inorganic materials:  
synthesis of methacrylic acid by supported gold  
catalysts and formation of vinylene carbonate by  
cathode active materials of lithium-ion batteries**

Yi-Fei Qiu

Department of Chemistry

January 2023

# Contents

<b>Chapter 1. General Introduction</b> .....	1
<b>1.1. Reference</b> .....	2
<b>Chapter 2. Oxidative Decomposition Mechanism of Ethylene Carbonate on Positive Electrodes in Lithium-Ion Batteries</b> .....	3
<b>2.1. Introduction</b> .....	3
<b>2.2. Experimental</b> .....	4
<b>2.2.1 Chemicals and Materials</b> .....	4
<b>2.2.2. Preparation of the Charged <math>\text{Li}_{1-x}\text{CoO}_2</math> Electrode</b> .....	5
<b>2.2.3. Preparation of Electrolyte</b> .....	5
<b>2.2.4. Synthesis of Reference Standards</b> .....	5
<b>2.2.5. Experimental Procedure for Electrolyte Reaction with Charged <math>\text{Li}_{1-x}\text{CoO}_2</math> Electrode</b> .....	7
<b>2.2.6. Analytical Method</b> .....	8
<b>2.3. Results and Discussion</b> .....	9
<b>2.3.1. Decomposition Products of Electrolyte and Influence from <math>\text{LiPF}_6</math></b> .....	9
<b>2.3.2. Investigation of Oxidation Reaction Mechanism by which EC Generates VC</b> .....	12
<b>2.4. Conclusions</b> .....	27
<b>2.5. NMR Charts</b> .....	28
<b>2.6. Reference</b> .....	33
<b>Chapter 3. Liquid Phase Oxidation of Methacrolein into Methacrylic Acid with Supported Au Catalysts</b> .....	35
<b>3.1. Introduction</b> .....	35
<b>3.2. Experimental</b> .....	36
<b>3.2.1. Chemicals and Materials</b> .....	36
<b>3.2.2. Preparation of Catalyst</b> .....	37
<b>3.2.2.1. Preparation of Monometallic Samples</b> .....	37

<b>3.2.2.2. Preparation of Bimetallic Samples</b> .....	37
<b>3.2.3. Characterization Techniques</b> .....	38
<b>3.2.4. Catalytic Activity</b> .....	39
<b>3.2.5. Precipitate Polymers of MAL and MAA which are By-products</b> .....	39
<b>3.3. Results and Discussion</b> .....	40
<b>3.3.1. Searching for Optimal Catalyst and Catalytic Performance</b> .....	40
<b>3.3.1.1. Optimizing Supported Au Catalyst and Reaction Time</b> .....	40
<b>3.3.1.2. Confirmation of Base Additive Effect</b> .....	42
<b>3.3.1.3. Examination of Alkaline Earth Metals as Secondary Metals</b> .....	43
<b>3.3.1.4. Examination of Transition Metals as Secondary Metals</b> .....	46
<b>3.3.2. Characterization of Catalyst</b> .....	48
<b>3.4. Conclusions</b> .....	60
<b>3.5. Reference</b> .....	61
<b>Acknowledgement</b> .....	64

## Chapter 1. General Introduction

In general, an oxidation reaction is a reaction in which a molecule, atom or ion loses electrons, or the oxidation state increases. In contrast, reduction reaction is a reaction with decreased oxidation state. Although these two reactions can be defined separately, these processes can also be referred to as redox reactions, as they often occur simultaneously. Oxidation reactions touch all aspects of daily life. For example, respiration which are vital to life for animals and plants, combustion of substances and corrosion of food are naturally common oxidation reactions. In these processes, movement of electrons occurs frequently. New compounds were synthesized through redox reactions by adding functional groups in existing compounds, thereby contributing to enriching lives. Among these, lithium-ion batteries that could store electricity, which are already indispensable for daily life. However, although lithium-ion batteries have been industrialized, there are still some problems have not been solved, such as lower thermal stability [1.1]. In particular, a large amount of heat is released during the rapid charging process which could promote chemical reactions in the cell, and the stability of electrolyte has become a major problem. On the other hand, high-potential cathodes are being studied to increase the energy density of batteries. However, the oxidation stability of the electrolyte will be decreased if the cathode potential increases to 4.5 V or more, then it would become more susceptible to oxidation. Therefore, a new electrolyte or electrolyte additive with high stability is important for the development of next-generation batteries with high energy density. In Chapter 2, the oxidative decomposition products of ethylene carbonate (EC)/ dimethyl carbonate (DMC) and the formation mechanism were explored using the cathode  $\text{LiCoO}_2$  (4.5 V), which could provide new insights into the design of electrolytes.

In another word, polycarbonate, which is a polymer of carbonate, is a kind of raw material for organic glass [1.2]. However, it cannot be widely used because of the bad weather resistance and high cost. Therefore, an acrylic organic glass made from methyl methacrylate (MMA) could be expected. Currently, MAA, a raw material for MMA, whose production processes are different from company to company, but all processes from toxic-free light hydrocarbons (such as ethylene, propylene and isobutane) rely on heterogeneous catalysts [1.3]. However, when the intermediate product methacrolein (MAL) is oxidized to MAA, there are problems of high reaction temperature ( $>300^\circ\text{C}$ ) and short catalyst life (heteropoly acid catalysts), which also leads to high cost. In Chapter 3, a new

selective oxidation catalyst was investigated. It can selectively oxidize MAL under milder reaction conditions, ranging from monometallic Au-supported catalysts to bimetallic Au-supported catalysts. The present study is meaningful to provide a new catalyst design route for MAL oxidation catalysts.

### 1.1. Reference

- [1.1] Ren, D.; Hsu, H.; Li, R.; Feng, X.; Guo, D.; Han, X.; Lu, L.; He, X.; Gao, S.; Hou, J.; Li, Y.; Wang, Y.; Ouyang, M. *eTransportation* **2019**, *2*, 100034.
- [1.2] Carrión, F.J.; Sanes, J.; Bermúdez, M. D. *Wear* **2007**, *262*, 1504.
- [1.3] Darabi Mahboub, M. J.; Dubois, J.L.; Cavani, F.; Rostamizadeh, M.; Patience, G. S. *Chem. Soc. Rev.* **2018**, *47*, 7703.

## **Chapter 2. Oxidative Decomposition Mechanism of Ethylene Carbonate on Positive Electrodes in Lithium-Ion Batteries**

### **2.1. Introduction**

Lithium-ion batteries (LIBs) have a higher energy density than other commercially available rechargeable batteries and are widely used in small electronic devices like mobile phones. In the context of the current global warming crisis and shortage of fossil fuels, there is an urgent demand to develop LIBs with a high-energy-density that can be used in large-scale installation such as electric vehicles. However, the safety of LIBs is an issue, because they can ignite and explode, leading to accidents. Traditional LIBs employ electrolytes in which lithium salts, as  $\text{LiPF}_6$  etc., are dissolved in organic solvents, which such as ethylene carbonate (EC) and dimethyl carbonate (DMC). When the valence of transition metals in the active materials contained in the positive electrode increases upon the charging of a LIB, the electrolyte easily reacts with the surface of the charged active materials (e.g.,  $\text{LiCoO}_2$ ) [1.1]. Venkatraman et al. have reported that oxygen lost from the lattice of  $\text{LiCoO}_2$  and  $\text{LiNi}_{0.85}\text{Co}_{0.15}\text{O}_2$  as an oxidant reacts with the electrolyte for charge compensation [1.2]. The released oxygen reacts with the electrolyte and then produces carbon dioxide gas [1.3]. These gaseous decomposition products from carbonate esters, leads to the expansion of the battery pack, which may cause leakage or ignition [1.4]. Furthermore, although electrolyte of  $\text{LiPF}_6$  is the most widely used caused by the excellent properties, it decomposes in the presence of trace amounts of water, producing phosphoric acid derivatives and hydrogen fluoride gas [1.5]. Therefore, understanding the decomposition mechanism is very important to further improve the safety of LIBs.

Theoretical studies on the mechanism of electrolyte solution decomposition reactions in charged LIBs have been reported. For the oxidation in the bulk electrolyte, Borodin et al. proved that oxidation occurs when hydrogen was removed from one EC molecule to another at a cathode with a potential  $>5.0$  V by conducting theoretical studies using quantum chemical calculations [1.6]. For oxidation occurring on positive electrode active materials, by density functional theory (DFT) calculations, Shao-Horn et al., the cleavage of C–H bonds of EC, which was a favorable process on the surface of several kinds of oxides (including  $\text{LiCoO}_2$ ) was reported [1.7]. After C–H bond cleavage, the formation of acetaldehyde,  $\text{CO}_2$ , and ring-opened EC dimers has been proposed [1.8]. Grey et al. conducted nuclear magnetic resonance (NMR) spectroscopy studies and detected the production of

glycolic acid as an oxidation product from EC with  $\text{LiCoO}_2$ . They found that chemical oxidation due to the loss of oxygen from the oxide is favorable to electrochemical oxidation [1.9]. Frieberg et al. succeeded in the *operando* detections of singlet oxygen when the potential state of  $\text{LiNi}_x\text{Co}_y\text{Mn}_z\text{O}_2$  ( $x + y + z = 1$ ) was increased to  $>5$  V [1.10]. They performed experiments where singlet oxygen was generated in situ by the photoexcitation of Rose Bengal and reacted with a mixed EC/DMC solvent, with  $\text{CO}_2$ , CO, and  $\text{O}_2$  being detected. The decomposition process of EC was also verified by conducting DFT calculations. Notably, vinylene carbonate (VC) and hydrogen peroxide ( $\text{H}_2\text{O}_2$ ) were produced in a one-step concerted mechanism through EC forms a six-membered ring transition state with singlet oxygen [1.3]. Shao-Horn et al. also confirmed the oxidation of EC to VC when Ni-based oxide was employed as a cathode material by in situ Fourier-transform infrared (FT-IR) spectroscopy and they proposed that the reaction occurs at the electrode surface [1.11]. Our present paper mainly describes the oxidation of EC to VC, which may be related to these studies. For the detection of the reaction intermediates, X-ray photoelectron spectroscopy is useful for the detection of salt-based products, such as  $\text{LiF}$ ,  $\text{Li}_x\text{F}_y^-$ , and  $\text{Li}_x\text{PO}_y\text{F}_z^-$  [1.12–1.14]. However, the high-vacuum conditions required for the measurements are inappropriate for measuring volatile organic compounds. Moreover, Nowak et al. through the means of isotopic labeling ( $^{13}\text{C}_3$ -EC,  $\text{D}_4$ -EC) investigated the Mechanism of gaseous decomposition products generated during the initial charge-discharge cycles [1.15]. Nevertheless, there have been little research on identifying decomposed organic products related to the kinetics and stereochemistry that are dissolved in electrolyte solution.

In this study, electrochemical reactions were not explored to simplify the research system. For the focus of our research, the decomposition reaction of carbonate esters was examined in contact with charged  $\text{Li}_{1-x}\text{CoO}_2$ .

## 2.2. Experimental

### 2.2.1 Chemicals and Materials

Dimethyl carbonate (DMC, battery-grade purity, 99.5%), propylene carbonate (PC for electrochemistry), and a mixed solution of ethylene carbonate / dimethyl carbonate (EC/DMC = 1/1, vol/vol) were purchased from Kanto Chemical CO., Inc. Ethylene-D4 carbonate (EC-D4, 98%), super dehydrated dichloromethane, and tridecane were purchased from FUJIFILM Wako Pure Chemical



Corporation. Vinylene carbonate (VC, battery-grade purity, 98%) was purchased from Tokyo Chemical Industry Co., Ltd. lithium hexafluorophosphate (LiPF<sub>6</sub>, 99.9%) was purchased from Kishida Chemical Co., Ltd. Lithium difluorophosphate (LiPO<sub>2</sub>F<sub>2</sub>, 98%) was purchased from Angene Chemical (China). Sodium monofluorophosphate (NaPO<sub>3</sub>F, 94%) was purchased from Strem Chemicals (USA).

For the thermal aging experiments, polypropylene vials were used from Maruemu Corporation.

### 2.2.2 Preparation of the Charged Li<sub>1-x</sub>CoO<sub>2</sub> Electrode

Cathode electrodes were prepared by mixing lithium cobalt oxide (Aldrich, 99.8%) with a small amount of conductive carbon additive and polyvinylidene fluoride (PVDF) binder dispersed in *N*-methylpyrrolidinone (NMP), and then the slurry was applied to an aluminum foil current-collector and then dried at 120°C under vacuum overnight.

Li<sub>1-x</sub>CoO<sub>2</sub> were prepared from the cathode electrodes by electrochemical delithiation. A coin-type cell with lithium metal foil of 1 mm thickness was assembled as a counter anode electrode where a polyethylene separator of 20 μm thickness was placed between the cathode and the lithium metal foil. Subsequently, the electrolyte solution of 1 mol/kg LiPF<sub>6</sub> dissolved in EC/DMC = 3/7 by weight was injected into the assembled cell. The cells were charged at a constant current density of 0.1 C to 4.5 V, 4.3 V, 4.1 V, and constant voltage until the current reached 1/50 C at room temperature. Charged cathodes were taken from the dismantled coin-cell and immediately washed with DMC.

### 2.2.3 Preparation of Electrolyte

LiPF<sub>6</sub> was dissolved in EC/DMC, VC/DMC, and DMC, respectively. The concentration of LiPF<sub>6</sub> in the electrolyte was 1 mol kg<sup>-1</sup>. EC/DMC containing 1 mol kg<sup>-1</sup> LiPO<sub>2</sub>F<sub>2</sub> and NaPO<sub>3</sub>F respectively were also prepared. The preparation of electrolytes was handled in a glove box with a N<sub>2</sub> atmosphere (O<sub>2</sub> ≤ 100 ppm, H<sub>2</sub>O < 300 ppm).

### 2.2.4. Synthesis of Reference Standards

#### 2.2.4.1. Synthesis of Methylvinylene Carbonate [1.16]

This compound was obtained in two steps from hydroxyacetone. Triphosgene (5.9 g, 20 mmol) was added to a cold (0°C) solution of dichloroethane (36 mL) containing hydroxyacetone, followed N, N-

dimethylaniline (6.8 g, 7.1 mL, 56 mmol) was added dropwise, while maintaining the temperature below 8°C. The mixture was stirred for 15 min at 0°C, then more two hours at rt. The mixture was cooled to 5°C, then Transfer it to a separatory funnel, and washed with cold 3 M aqueous hydrochloric acid, water, and brine, and dried by NaSO<sub>4</sub>. After filtered and concentrated at the rotary evaporator to the half of the initial volume. The residue was heated to reflux for three hours. The solvent was completely removed at the rotary evaporator, and the remaining oil was heated under argon to 170°C, for two and half hours, when considerable darkening occurs. The crude mixture was distilled under reduced pressure, to give methylvinylene carbonate (IUPAC name: 4-methyl-1,3-dioxol-2-one), which is a light-yellow oil.

<sup>1</sup>H NMR (400 MHz, CD<sub>3</sub>OD): 7.13 (q, *J* = 1.6 Hz, H); 2.10 (d, *J* = 1.6 Hz, 3H). <sup>13</sup>C NMR (100 MHz, CD<sub>3</sub>OD): 155.3 (C); 142.9 (C); 127.9 (CH); 9.6 (CH<sub>3</sub>).

#### **2.2.4.2. Synthesis and Discussion of Deuterium-substituted EC in the Stereochemistry of Syn (syn-EC-D2)**

To obtain further evidence of whether the hydrogens were eliminated in syn stereochemistry during the reaction from EC to VC, the stereochemistry elimination reaction was investigated using syn-EC-D2.

Syn-EC-D2 was synthesized and analyzed by atmospheric pressure solid analysis probe mass spectrometer (ASAP-MS) (Figure 4). Generally, the hydrogenation reaction should proceed with syn stereochemistry, we also conducted an experiment to confirm the relative configuration and purity of the synthesized syn-EC-D2.

EC molecule has an axis of symmetry, and the four hydrogens have the same geometric configuration, so they are equivalent and only one peak is visible in <sup>1</sup>H NMR. However, if the intramolecular symmetry is broken, inequivalent compounds can be derived and hydrogen can be distinguished, therefore, EC-D2 was ring-opened and converted to ethylene glycol (EG), which was used to acetalize with camphor. As a result, the four hydrogens in the acetal moiety became unequal and could be distinguished by NMR (Figure 15, 16). Detailed synthesis methods are as follows:

#### 2.2.4.2.1. Synthesis of syn-EC-D2

Chlorotris(triphenylphosphine)rhodium(I) (0.8 g, 0.9 mmol) was introduced in vinylene carbonate (0.8 g, 9.3 mmol) at 60°C, under D<sub>2</sub> (1.5 MPa) stirred for 24 h. The residue was purified by silica-gel column to give EC-D2.

Chlorotris(triphenylphosphine)rhodium(I) was prepared by the literature method [1.17].

<sup>1</sup>H NMR (600 MHz, CDCl<sub>3</sub>): 4.51 (s, 2H). <sup>13</sup>C NMR (150 MHz, CDCl<sub>3</sub>): 155.4 (C); 64.2 (t, *J* = 23.0 Hz, 2C).

#### 2.2.4.2.2. Synthesis of 1,7,7-Trimethylspiro[bicyclo[2.2.1]heptane-2,2'-[1.3]dioxolane] (D2)

EC-D2 (0.09 g, 1 mmol), Na<sub>2</sub>CO<sub>3</sub> (10 wt%, 0.009 g), and H<sub>2</sub>O (0.028 g, 1.6 mmol) were introduced in MeOH (0.6 ml) at 60°C, and stirred for 8h to give ethylene glycol (D2). Then, the residue and triethyl orthoformate (0.22 g, 1.5 mmol), *p*-toluenesulfonic acid (0.02 g, 0.1 mmol), and (±)-1,7,7-trimethylbicyclo[2.2.1]heptan-2-one (0.23 g, 1.5 mmol) were introduced in 1 ml of benzene/toluene (7/3, vol/vol) at 40°C for 48 h to give 1,7,7-trimethylspiro[bicyclo[2.2.1]heptane-2,2'-[1,3]dioxolane] (D2). The residue was purified by silica-gel column.

<sup>1</sup>H NMR (600 MHz, CDCl<sub>3</sub>): 3.84 (d, *J* = 6.0 Hz, 0.5H), 3.77 (d, *J* = 7.2 Hz, 0.5H), 3.73 (d, *J* = 6.0 Hz, 0.5H), 3.65 (d, *J* = 7.2 Hz, 0.5H), 1.97 (dd, *J* = 4.8, 3.6, 0.5H), 1.94 (dd, *J* = 4.8, 3.6, 0.5H), 1.82 (m, 1H), 1.63 (m, 2H), 1.32 (m, 2H), 1.13 (m, 1H), 0.94 (s, 3H), 0.77 (s, 3H), 0.72 (s, 3H). <sup>13</sup>C NMR (150 MHz, CDCl<sub>3</sub>): 117.3 (C), 64.6 (t, *J* = 23.0 Hz, C), 63.4 (t, *J* = 23.0 Hz, C), 52.2 (C), 48.1 (C), 45.0 (C), 44.7 (C), 29.6 (C), 27.0 (C), 20.5 (C), 20.4 (C), 9.96 (C).

#### 2.2.5 Experimental Procedure for Electrolyte Reaction with Charged Li<sub>1-x</sub>CoO<sub>2</sub> Electrode

Charged Li<sub>1-x</sub>CoO<sub>2</sub> electrode (90 mg) removed from a battery was washed by DMC three times, dried, and then introduced in 1.6 mL of electrolyte in a bottle made of polypropylene. The charged voltages were set at 4.5 V, 4.3 V, and 4.1 V, respectively. The materials were handled in the glove box with an Ar atmosphere (O<sub>2</sub> ≤ 100 ppm, H<sub>2</sub>O < 300 ppm). The mixture was kept at 50°C with a hotplate and sampled in the glove box. The reaction products of the sample were analyzed using Gas Chromatography (GC) and GC-MS.

In addition, an electrolyte containing LiPF<sub>6</sub> was also evaluated in a similar manner. More concretely,

the removed electrode was soaked in 100  $\mu$ L of the electrolyte, and then was sealed in a bottle made of polypropylene. The mixture was kept at 50°C. After heating, the sample was opened in the glove box, and was added tridecane (internal standard) and  $\text{CH}_2\text{Cl}_2$  (3 mL). The residue mixture was cooled in the freezer for 1 h and filtered. The materials were handled in the glove box with an  $\text{N}_2$  atmosphere ( $\text{O}_2 \leq 100$  ppm,  $\text{H}_2\text{O} < 300$  ppm).

### 2.2.6 Analytical Method

$^1\text{H}$  NMR (400 MHz and 600 MHz),  $^{13}\text{C}$  NMR (100 MHz and 150 MHz),  $^{19}\text{F}$  NMR (376 MHz), and  $^{31}\text{P}$  NMR (162 MHz) spectra were recorded in chloroform-D, methanol-D4, and acetone-D6 on a JEOL JNM-ECS400 spectrometer and JEOL JNM-ECA600 spectrometer. Multiplicity was indicated as follows: s (singlet), d (doublet), t (triplet), q (quartet), quin (quintet), sext (sextet), sept (septet), m (multiplet), br (broad). Chemical shifts for  $^1\text{H}$  NMR were reported in ppm and referenced to the center line of a singlet at 7.26 ppm for chloroform-D, a quintet at 3.31 ppm for methanol-D4, and a quintet at 2.05 ppm for acetone-D6, respectively. Chemical shifts for  $^{13}\text{C}$  NMR were referenced to the center line of a triplet at 77.16 ppm for chloroform-D, a sept. at 49.00 ppm for methanol-D4, and a sept. at 29.84 ppm for acetone-D6, chemical shifts for  $^{19}\text{F}$  and  $^{31}\text{P}$  NMR are reported in ppm and referenced to trifluoromethylbenzene (at  $-63.72$  ppm for  $^{19}\text{F}$  NMR) and 85%  $\text{H}_3\text{PO}_4$  in  $\text{D}_2\text{O}$  as an external standard (at 0 ppm for  $^{31}\text{P}$  NMR), respectively.

The electrolytes reacted with  $\text{Li}_{1-x}\text{CoO}_2$  were analyzed by GC (Agilent GC 6850 Series II equipped with FID), and GC-MS (Thermo Fisher Scientific Polaris Q using electron impact [ $\text{EI}^+$ ] ionization mode), both were equipped with a same J&W HP-INNOWAX column (0.25  $\mu\text{m}$  thickness, 0.25 mm I.D., 30 m.)

Measurement of mass spectrometry of deuterium-substituted EC in the stereochemistry of syn (syn-EC-D2) was performed on Waters SQ Detector 2. The source temperature was 120°C, probe temperature was 400°C. Corona electric current was 5.00 A, corona voltage was 1.5 V, and cone voltage was 71.00 V. atmospheric pressure solid analysis probe (ASAP) positive ionization mode was used.

## 2.3. Results and Discussion

### 2.3.1. Decomposition Products of Electrolyte and Influence from LiPF<sub>6</sub>

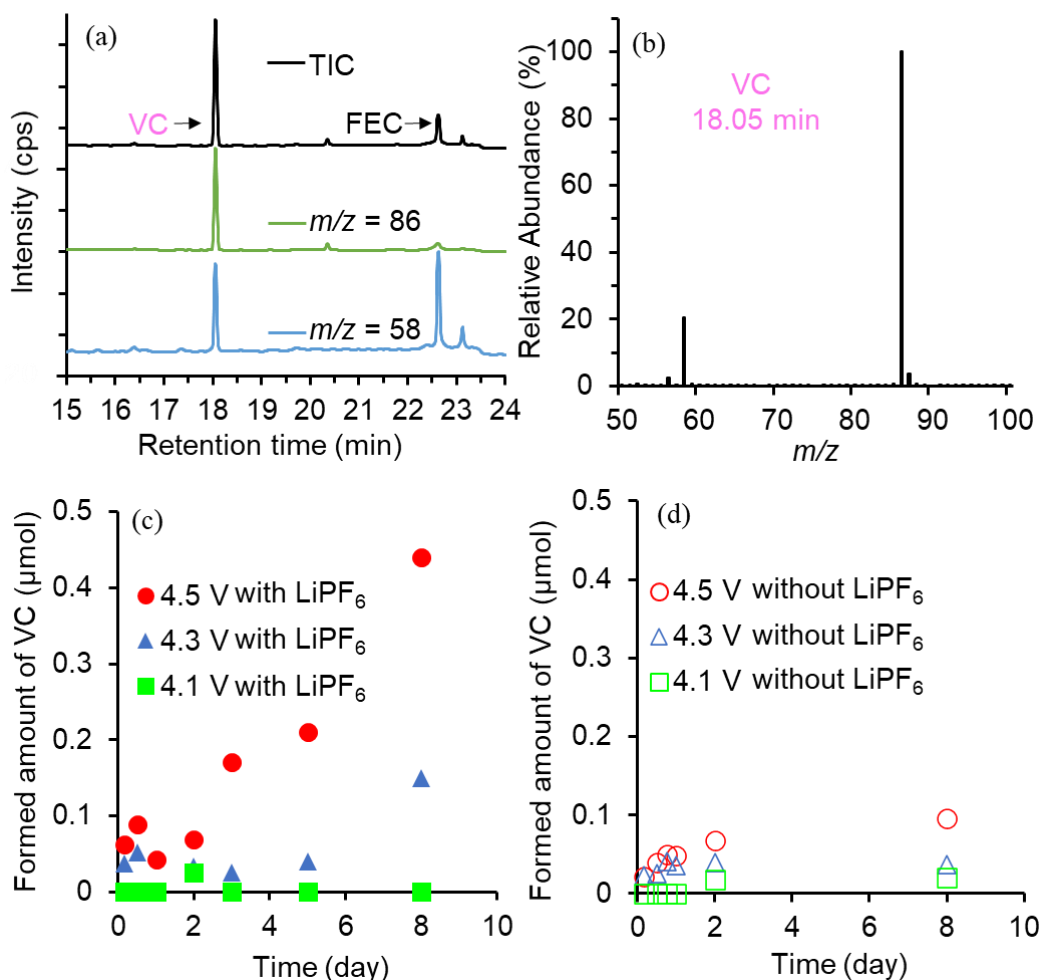


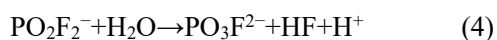
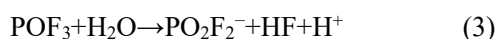
**Figure 1.** (a) GC-MS chromatogram of the filtered solution from EC/DMC (1/1, vol/vol) containing LiPF<sub>6</sub> (1 mol kg<sup>-1</sup>) with Li<sub>1-x</sub>CoO<sub>2</sub> (4.5 V) at 50°C for two days and the characteristic mass fragments:  $m/z = 86$  and 58 for VC, (b) mass spectrum corresponding to the peak of VC observed at 18.05 min on the total ion chromatogram (TIC), (c) time course of the amount of VC in EC/DMC/Li<sub>1-x</sub>CoO<sub>2</sub> (4.5 V, 4.3 V, and 4.1 V) with LiPF<sub>6</sub> and (d) without LiPF<sub>6</sub>.

Several kinds of decomposition products were detected on GC from the electrolyte, and VC is in perfect agreement at MS. VC was detected after the retention time of 18.1 min in GC-MS chromatogram as shown in Figure 1a. The corresponding mass spectra are shown in Figure 1b. DMC and the diluting solvents were detected within 5 min, fluoroethylene carbonate (FEC) after 22.6 min,

and EC after 25 min. Among the several detected peaks, the behavior and formation mechanism of VC were investigated. In addition, several products from LiPF<sub>6</sub> were detected on NMR as shown in Figure 12 and Figure 13.

The amounts of produced VC were compared for the reaction in EC/DMC/Li<sub>1-x</sub>CoO<sub>2</sub> in the presence or absence of LiPF<sub>6</sub> (Figures 1c and 1d). The charge potentials of Li<sub>1-x</sub>CoO<sub>2</sub> were determined to be 4.5 V, 4.3 V, and 4.1 V, respectively. When the charged potential was 4.5 V, a particularly large amount of VC was produced. On the contrary, the decomposition of EC did not proceed at all with the charged potential 4.1 V. In an interesting point, VC generation was accelerated in the presence of LiPF<sub>6</sub>. An actual battery system has electrolyte such as LiPF<sub>6</sub>, where they interact with the electrolyte solution and cause decomposition. In 2013, Hu et al. analyzed the EC decomposition path by conducting DFT calculations and reported that the decomposition products of EC differ depending on if anions such as PF<sub>6</sub><sup>-</sup> and ClO<sub>4</sub><sup>-</sup> are present [1.18]. This work suggests that if an anion is present, the Li-EC-anion complex will be easily oxidized compared to free EC due to the lower redox potentials of the complexes, such as EC-PF<sub>6</sub><sup>-</sup> and EC-ClO<sub>4</sub><sup>-</sup>, formed in the reaction system; Therefore, when LiPF<sub>6</sub> exist, the decomposition pathway of EC may change.

In addition, LiPF<sub>6</sub> can be unstable in the solution. Schmutzler et al. reported that PF<sub>6</sub><sup>-</sup> can give PO<sub>3</sub>F<sub>2</sub><sup>-</sup> and PO<sub>2</sub>F<sub>2</sub><sup>-</sup> with a small amount of water [1.19], as following equations (1) – (4):



To confirm the possibility of LiPF<sub>6</sub> decomposition in the present system, an EC/DMC solution with LiPF<sub>6</sub> (1 mol kg<sup>-1</sup>) was stored at a temperature of 50°C for 8 days, subsequently through <sup>19</sup>F and <sup>31</sup>P NMR spectroscopies, the decomposition species in the solution was determined [1.19]. PO<sub>3</sub>F<sub>2</sub><sup>-</sup> and PO<sub>2</sub>F<sub>2</sub><sup>-</sup> were found in the solution although PF<sub>6</sub><sup>-</sup> was still the major component (Figures 12 (a) and 13 (a)), indicating that trace amount of hydrolysis actually happened during the 8-days-storage. In

contrast, when charged  $\text{Li}_{1-x}\text{CoO}_2$  was present, only  $\text{PF}_6^-$  could be observed (Figures 12 (b) and 13 (b)). In other words, the NMR signals of  $\text{PO}_3\text{F}^{2-}$  and  $\text{PO}_2\text{F}_2^-$  had disappeared when  $\text{Li}_{1-x}\text{CoO}_2$  was immersed in the solution in which  $\text{LiPF}_6$  was hydrolyzed in advance. The origin of water has not yet been fully understood but may be related to the eliminated hydrogen in the reaction of EC into VC as  $\text{Li}_{1-x}\text{CoO}_2$  probably acts as an oxidant during the storage.

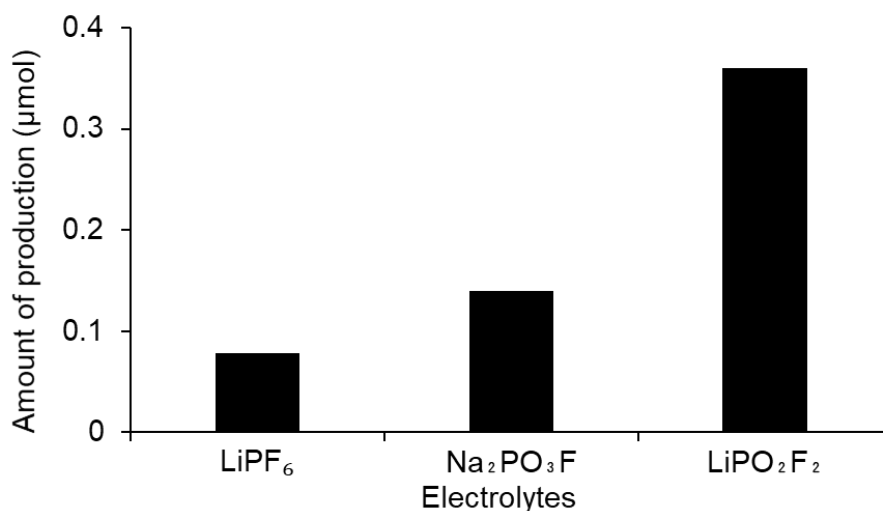


**Figure 2.** Amount of VC production in the presence of  $\text{LiPF}_6$ ,  $\text{LiPO}_2\text{F}_2$ , and  $\text{Na}_2\text{PO}_3\text{F}$  under the condition of  $50^\circ\text{C}$  for two days.

To understand the contributions of  $\text{PO}_3\text{F}^{2-}$  and  $\text{PO}_2\text{F}_2^-$  to the EC decomposition,  $\text{LiPO}_2\text{F}_2$  or  $\text{Na}_2\text{PO}_3\text{F}$  was dissolved into EC/DMC instead of  $\text{LiPF}_6$ , and the amount of VC production of each solution was quantified under the same conditions as the other experiments. Here commercially available  $\text{Na}_2\text{PO}_3\text{F}$  was used instead of unavailable  $\text{Li}_2\text{PO}_3\text{F}$ .

As shown in Figure 2, when  $\text{Na}_2\text{PO}_3\text{F}$  was added ( $1 \text{ mol kg}^{-1}$ ) to the EC/DMC electrolyte in the presence of the charged  $\text{Li}_{1-x}\text{CoO}_2$ , and  $0.14 \text{ } \mu\text{mol}$  of VC was formed in two days. This indicates a subtle promotion effect was observed for VC formation. A more obvious acceleration effect (generating  $0.36 \text{ } \mu\text{mol}$  of VC) was observed in the formation of VC when  $\text{LiPO}_2\text{F}_2$  was added. As reported by Lei et al., the  $\text{EC-PO}_2\text{F}_2$  which exist in the solution of EC and  $\text{LiPO}_2\text{F}_2$ , is more easily oxidized than EC alone [1.20]. However, when only  $\text{LiPF}_6$  was added, only  $0.08 \text{ } \mu\text{mol}$  of VC was obtained; Therefore, it is suggested that  $\text{PO}_2\text{F}_2^-$  and  $\text{PO}_3\text{F}^{2-}$  contribute to the acceleration of the VC formation compared to  $\text{PF}_6^-$ . Clarifying the decomposition of electrolyte which is a complex

compound is a future work. On the other hand, it was assumed that the decomposition of  $\text{LiPF}_6$  has not yet occurred where the reaction time was relatively short (0–2 days).

### 2.3.2 Investigation of Oxidation Reaction Mechanism by Which EC Generates VC

To understand the process of the oxidation of EC in VC generation, firstly, the C–H bond cleavage mechanism of EC was studied according to the kinetic isotope effect (KIE). In this reaction, VC is generated regardless of the presence or absence of  $\text{LiPF}_6$ , but the reaction was examined in the absence of  $\text{LiPF}_6$  to minimize its effect in present study. Literature reports have shown that VC may be formed from EC in three ways: (a) concerted dihydrogen abstraction with singlet oxygen, as suggested by DFT calculations [1.3], (b) dehydrogenation on a Ni-based oxide in a LIB [1.11], and (c) radical monochlorination of EC [1.21]; moreover, there had some literature Research of elimination of hydrogen chloride [1.22, 1.23]. In the first way, a concerted dihydrogen abstraction reaction (a), Freiberg et al. had reported that EC reacts with singlet oxygen through a six-membered ring transition state to form VC (Figure 9). In the second way, although the detailed mechanism is still unknown, VC formation was observed by in situ IR spectroscopy in a  $\text{LiNi}_{0.8}\text{Co}_{0.1}\text{Mn}_{0.1}\text{O}_2$  (NCM811) surface at voltages of as low as 3.8 V.

In the third way of a radical reaction, C–H bond cleavage takes place, which also seems to be a possible process in the reaction of VC formation was reported in this present study. Therefore, KIEs were investigated to gain mechanistic insights into this process. Figure 3a shows the time course of the concentration of VC-H2 and VC-D2, whose structure formulas are shown in the inset. Both of the observed amounts are rather small comparing with the EC and deuterium-labeled EC-D4 (<0.1%) used as a starting material. This suggests that the reaction is at a very early stage. Therefore, if the reaction rate is dependent only on the concentration of EC, the amount of VC should increase linearly regardless of the reaction of EC. However, the actual reaction rates slightly decrease with time, possibly because the reaction rate is also dependent on the oxidizing species on  $\text{Li}_{1-x}\text{CoO}_2$ , and the amount of it also decreases [1.24]. The reaction rates were calculated to be  $1.74 \times 10^{-4} \text{ mol L}^{-1} \text{ day}^{-1}$  (VC-H2) and  $5.93 \times 10^{-5} \text{ mol L}^{-1} \text{ day}^{-1}$  (VC-D2) using the first five days' worth of data.



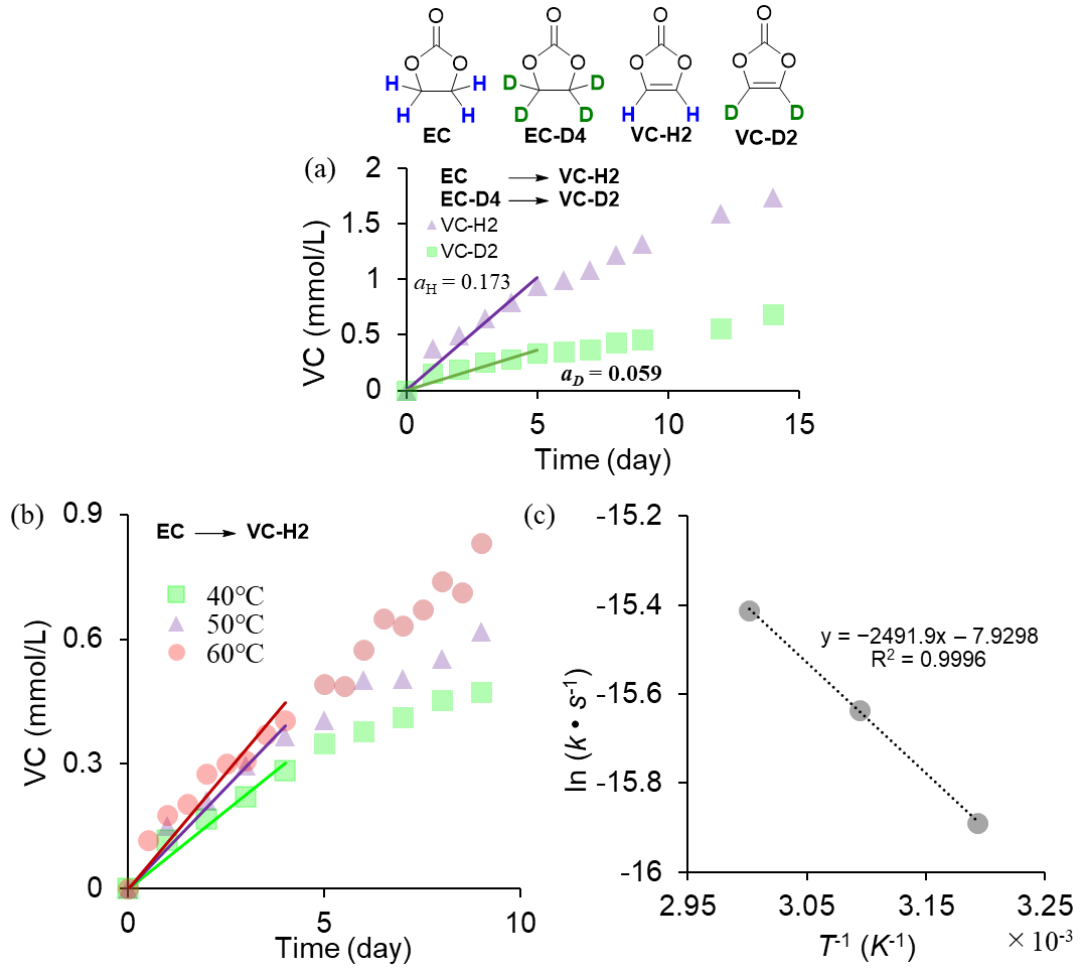


**Figure 3.** KIEs and Arrhenius plots of the reaction to form VC from EC in the presence of a  $Li_{1-x}CoO_2$  cathode. (a) Time courses of the amount of VC-H2 and VC-D2 at 50°C. (b) Time courses of the amount of VC-H2 on the  $Li_{1-x}CoO_2$  cathode at 40°C, 50°C, and 60°C. (c) Arrhenius plot of the reaction that results in the formation of VC-H2 on the  $Li_{1-x}CoO_2$  cathode.

The rate equations of VC (VC-H2) and VC-D2 are as follows:

$$k_H[EC][Ox] = d[VC]/dt \quad (5)$$

$$k_D[EC-D4][Ox] = d[VC-D2]/dt \quad (6)$$

where  $k_H$  and  $k_D$  are the reaction rate constants of EC and EC-D4, respectively, and [Ox] is the

concentration of the actual oxidizing active species. The relative ratio of these independently determined reaction rate constants ( $k_H/k_D$ ) was determined to be 2.9; thus, a typical KIE was observed. This result indicates that the C–H bond cleavage step was irreversible and corresponds to the rate-determining step of the overall process in this reaction [1.24].

To understand the detailed mechanism, the activation parameters of this reaction were estimated using the following equations, where Equation (9) is the Eyring equation:

$$a = -E_a/R \quad (7)$$

$$\Delta H^\ddagger = E_a - RT \quad (8)$$

$$\Delta G^\ddagger = RT \ln(xk_B T/kh) \quad (9)$$

$$\Delta S^\ddagger = (\Delta H^\ddagger - \Delta G^\ddagger)/T \quad (10)$$

where  $E_a$  is the activation energy,  $R$  is the gas constant,  $a$  is the slope of the Arrhenius plot,  $T$  is the temperature,  $h$  is Planck's constant,  $\Delta H^\ddagger$  is the activation enthalpy,  $\Delta G^\ddagger$  is the activation Gibbs energy,  $k_B$  is the Boltzmann constant,  $k$  is a reaction rate constant,  $x$  is the transmittance, and  $\Delta S^\ddagger$  is the activation entropy.

**Table 1. Details for calculating activation parameters.**

Days	Concentration (mmol L <sup>-1</sup> )				$k$ (s <sup>-1</sup> )
	1	2	3	4	
40°C	0.12	0.17	0.22	0.29	$1.26 \times 10^{-7}$
50°C	0.15	0.21	0.30	0.37	$1.62 \times 10^{-7}$
60°C	0.18	0.28	0.31	0.41	$2.03 \times 10^{-7}$

The reaction of EC with DMC and Li<sub>1-x</sub>CoO<sub>2</sub> was conducted at 40°C, 50°C, and 60°C, resulting in reaction rates of approximately  $8.68 \times 10^{-5}$  mol L<sup>-1</sup> day<sup>-1</sup>,  $1.12 \times 10^{-4}$  mol L<sup>-1</sup> day<sup>-1</sup>, and  $1.40 \times 10^{-4}$  mol L<sup>-1</sup> day<sup>-1</sup>, respectively (Figure 3b). These values were used to calculate VC generation rate constants ( $k$ ) which are shown in Table 1 and the values of  $k$  could construct an Arrhenius plot, as shown in Figure 3c. Using equations (7) – (10), the activation parameters were calculated, which are listed in Table 2.

The activation energy ( $E_a$ ) was determined by Arrhenius equation (Equations 11 and 12). Where frequency factor ( $A$ ) can be obtained from the slopes of the line in Figure 3c.

$$k = Ae^{-E_a/RT} \quad (11)$$

Taking the natural logarithm of the Arrhenius equation gives:

$$\ln k = -\frac{E_a}{RT} + \ln A \quad (12)$$

So, if  $1/T$  is regarded as  $x$ , the slope  $a$  can be rewritten as:

$$y = ax + b \quad (13)$$

So, the slope  $a$  can be rewritten as the equation (14) which is the same as equation (7):

$$a = -\frac{E_a}{R} \quad (14)$$

Other activation parameters were calculated by the Eyring equation (Equation 15). Transforming this equation into equation (9),  $\Delta G^\ddagger$  can be determined. Where  $x = 1$  was set (It means that all transition state molecules proceed to product formation). The Boltzmann and Planck constants were  $k_B = 1.381 \times 10^{-23} \text{ J K}^{-1}$  and  $h = 6.626 \times 10^{-34} \text{ J s}$ . Using the differential form of equation 15, in conjunction with equation 12, the equation (8) was obtained. The activation enthalpy ( $\Delta H^\ddagger$ ) can be determined.

$$k = \frac{xk_B T}{h} e^{-\Delta G^\ddagger/RT} \quad (15)$$

$\Delta H^\ddagger$  and  $\Delta G^\ddagger$  can be used to obtain the activation entropy  $\Delta S^\ddagger$  as shown in equation (10).

**Table 2.** Activation parameters estimated from the Arrhenius plot shown in Figure 3c.<sup>a</sup>

$E_a$ (kJ mol <sup>-1</sup> )	$\Delta H^\ddagger$ (kJ mol <sup>-1</sup> )	$\Delta G^\ddagger$ (kJ mol <sup>-1</sup> )	$\Delta S^\ddagger$ (J mol <sup>-1</sup> K <sup>-1</sup> )
20.7	18.0	121	-320

<sup>a</sup> For the calculation of  $\Delta G^\ddagger$  and  $\Delta S^\ddagger$  using the Eyring equation (9), the rate constant was calculated based on  $k_H[\text{Ox}] = d[\text{VC}]/dt$  and initial  $[\text{Ox}] = 0.008 \text{ mol L}^{-1}$ , see Table S1, S2 for the detailed calculation data.

Among these parameters (Table 2), the  $\Delta S^\ddagger$  value was the focus. Generally,  $\Delta S^\ddagger$  allows an estimation of the degree of freedom at the transition state of the reaction. The large negative  $\Delta S^\ddagger$  value of  $-320 \text{ J mol}^{-1} \text{ K}^{-1}$  in this reaction indicates that the transition state has a rigid structure. However, although it is not known whether the cathode surface features singlet oxygen or highly oxidized species, it is expected that there is a large excess of EC and less of the oxidizing active species. For this rate equation (Equation (5)), in any case, the process should be analyzed as a pseudo-first-order reaction, as shown in Equation (5)\*:

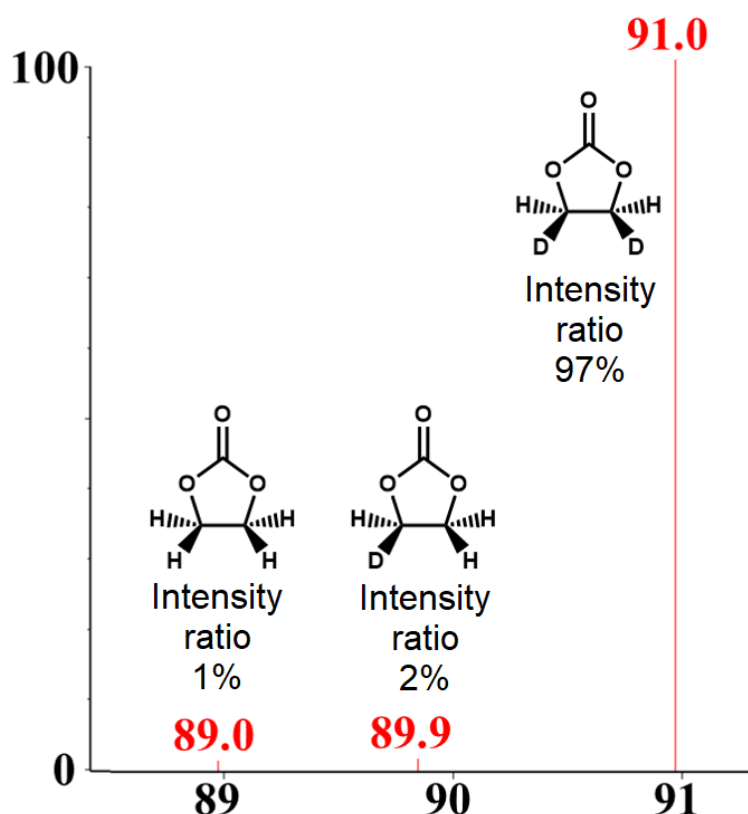
$$k_H[\text{Ox}] = d[\text{VC}]/dt \quad (5)^*$$

Although the actual oxidizing active species and their amount is not known, there should be at least  $2 \text{ mmol L}^{-1}$  in the current reaction system as the amount of VC is around this amount (Figure 3a), and is probably several times higher than this value. To estimate the  $\Delta G^\ddagger$  and  $\Delta S^\ddagger$  values using the Eyring equation (9), the rate constant was calculated by assuming the initial concentration of oxidizing active species to be  $8 \text{ mmol L}^{-1}$  (Tables 1 and 2). In the range of possible concentrations of oxidizing active species, the  $\Delta S^\ddagger$  values were calculated to be  $< -300 \text{ J mol}^{-1} \text{ K}^{-1}$  (Table 3). Using a larger value as the concentration of the active species increases the absolute value  $\Delta S^\ddagger$ . Although an impossibly large number, using the concentration of EC,  $7.5 \text{ mol L}^{-1}$  for the calculation gave a value of  $\Delta S^\ddagger$  of  $-377 \text{ J mol}^{-1} \text{ K}^{-1}$ .

**Table 3.** Activation parameters by simple calculations based on active species concentration.

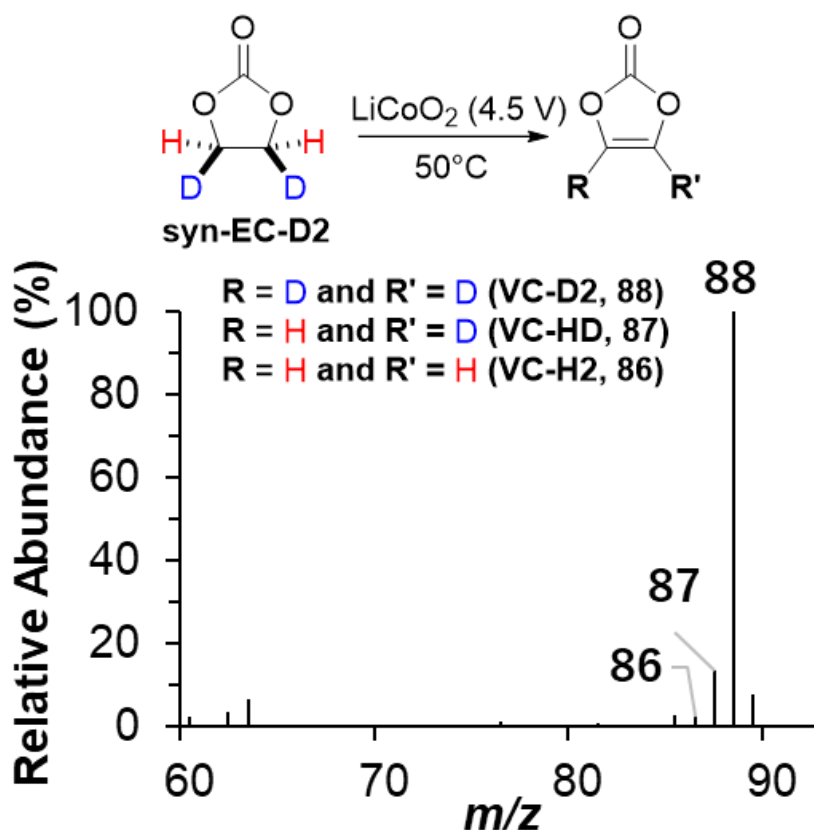
Active species concentration on $\text{Li}_{1-x}\text{CoO}_2$ ( $\text{mol L}^{-1}$ )	$E_a$ ( $\text{kJ mol}^{-1}$ )	$\Delta H^\ddagger$ ( $\text{kJ mol}^{-1}$ )	$\Delta G^\ddagger$ ( $\text{kJ mol}^{-1}$ )	$\Delta S^\ddagger$ ( $\text{J mol}^{-1} \text{K}^{-1}$ )
$[\text{Ox}] = 0.002$	20.7	18.0	118	-308
$[\text{Ox}] = 0.008$	20.7	18.0	121	-320
$[\text{EC}] = 7.5$ (instead of $[\text{Ox}]$ )	20.7	18.0	138	-377

In figure 2a, the observed amount of VC-H2 was around 0.002 mol/L after being reacted for 15 days. Therefore, the  $[\text{Ox}]$  in the pseudo-first-order reaction should be also more than 0.002 mol/L (equation (5)\*), and the actual reaction  $\Delta S^\ddagger$  should be lower than the calculated one ( $-308 \text{ J mol}^{-1} \text{K}^{-1}$ ).



**Figure 4.** Mass spectrometry of syn-EC-D2 synthesized by ASAP-MS.

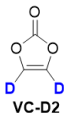
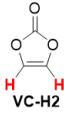
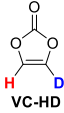
As VC could not be observed in the EC/DMC electrolyte without the addition of highly oxidized  $\text{Li}_{1-x}\text{CoO}_2$ , it was considered that the two hydrogens which were detached from EC, that were oxidatively eliminated by singlet oxygen derived from the highly oxidized  $\text{Li}_{1-x}\text{CoO}_2$ , or by its surface oxidizing species. To investigate the reaction mechanism in further detail, syn-EC-D2 was prepared through the hydrogenation of VC with  $\text{D}_2$ . The purity of syn-EC-D2 was 97% (Figure 4), accompanied by 2% EC-D1 and 1% EC, which was confirmed by ASAP-MS analysis and  $^1\text{H}$  NMR spectroscopy (Figures 4 and 14). The syn-stereospecificity of the hydrogenation was confirmed by  $^1\text{H}$  NMR analysis of the ethylene- $\text{D}_2$  acetal of ( $\pm$ )-camphor derived from syn-EC-D2 (Figures 15 and 16). In recent years, there have been numerous detailed investigations on C–H activation reactions, but typical reaction mechanisms, such as oxidative addition [1.25], electrophilic aromatic substitution (EAS) [1.26], and concerted metalation–deprotonation (CMD) [1.27], do not seem to be involved in this reaction owing to low-valent late-transition metals and aromatic compounds are not involved. For the radical elimination of hydrogen [1.28], generally,  $\Delta S^\ddagger$  has a positive value and the degree of freedom of the transition state is large, which is inconsistent with the results obtained in this study. In addition, when radical C–H activation is the rate-determining step, an increase in  $k_{\text{H}}/k_{\text{D}}$  is often observed [1.29–1.31]. However, the above-mentioned KIE has a normal value ( $\text{KIE} = 2.9$ ). For further confirmation, the stereochemistry of the elimination reaction was investigated using syn-EC-D2. If radical intermediates are generated from EC after hydrogen is eliminated, there is a high possibility that a non-stereospecific reaction takes place.



**Figure 5.** Mass spectrum of VC produced from syn-EC-D2.

The oxidation of syn-EC-D2 was conducted at 50°C using charged Li<sub>1-x</sub>CoO<sub>2</sub>. The molecular mass spectrometry of the obtained VC was inspected using GC-MS (Figure 5), where the major product was found to be VC-D2 with a mass number of 88, containing two deuteriums. In contrast, VC-H2, formed by the elimination of two deuteriums, accounted for only 1% of the detected species. The third product, VC-HD, was generated by the removal of one hydrogen and one deuterium. The intensity ratio of the three types of VC detected in the GC-MS data was 88:1:11 (Table 4). As a result, the percentage of VC produced by syn-elimination accounted for 89% (88% + 1%) of the product, with only around 11% of VC-HD produced via an anti-elimination reaction. The proportion of the products of the reaction was considered, assuming that stereospecific syn-elimination and non-stereospecific reactions take place. Typically, the former is an elimination reaction involving singlet oxygen and the latter is a radical reaction. In the latter case, the ratios of VC-D2, VC-H2, and VC-HD are assumed to be determined solely by deuterium KIEs.

**Table 4.** Component ratio of VC from mass spectrum

Molecular formula	<i>m/z</i>	Specific strength (%)	Elimination	Ratio (%)
 VC-D2	88	88	Syn	89
 VC-H2	86	1	Syn	
 VC-HD	87	11	Anti	11

Here, as already discussed,  $KIE = 2.9$  was observed in the independent experiments by measuring the reaction rates using EC and EC-D4, which means that the first C–H cleavage step is rate-limiting and irreversible. As the second step is not rate-limiting, the KIE value in the second step does not appear to show any difference in reaction rate, irrespective of if the reaction is stereospecific or non-stereospecific. However, it does affect the selectivity [1.24], and the ratios of VC-D2, VC-H2, and VC-HD changes.

When the reaction proceeds via a one-step concerted mechanism, as in the reaction with singlet oxygen [1.3], the value  $k_H/k_D = 2.9$  cannot be used to explain the selectivity (VC-D2:VC-H2 = 88:1) of the elimination of syn-EC-D2 (Figure 6). As Hartwig et al. pointed out [1.24], the KIE values are often not identical between the two parallel reactions and intramolecular competition. However, this is observed in multi-step mechanisms where the rate-limiting and C–H activation steps are different, and this is not the case for the concerted one-step reaction with singlet oxygen. Perhaps, if the reaction does proceed with singlet oxygen, the observed anti-elimination suggests that a somewhat more complicated process concurrently occurs.



## Concerted one-step elimination

$$k_H/k_D = 2.9$$

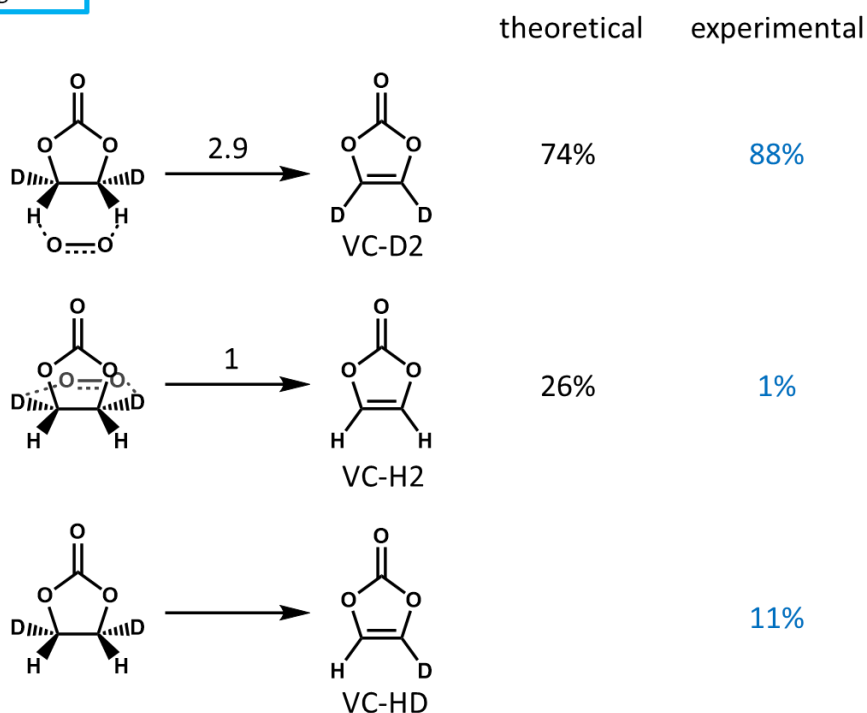


**Figure 6.** Proportions of isotopomers by simple calculations in VC-H2, VC-HD, and VC-D2 generated from syn-EC-D2 in the case of concerted one-step elimination based on the kinetic isotope effect ( $k_H/k_D = 2.9$ ).

Figure 7 shows schemes of the stereospecific two-step syn-elimination reaction under this assumption, where: (a)  $k_H/k_D = 2.9$  is assumed for both the first and second steps, (b) and (c)  $k_H/k_D = 10$  and 100 for the second step, respectively, are assumed. Although, it is not clear whether the oxidation reaction that occurs on the electrode surface is one-step or multi-step, which could be the case [1.11]. In case (c), the ratio of VC-D2 to VC-H2 becomes 96.7:1.6, which is close to the actual value of 88:1. However, VC-HD accounts for <2% in all cases (a–c), much lower than the actual value of 11%. This is because, in the case of stereospecific syn-elimination reactions, VC-HD is only produced from EC-D1, only 2% of which is present from the beginning. Therefore, completely stereospecific syn-elimination reactions alone cannot explain the ratio of the products from syn-EC-D2.

## Syn-elimination

$k_H/k_D = 2.9$  in 1st step,

$k_H/k_D = X$  in 2nd step

Assuming the 1st step is rate-determining

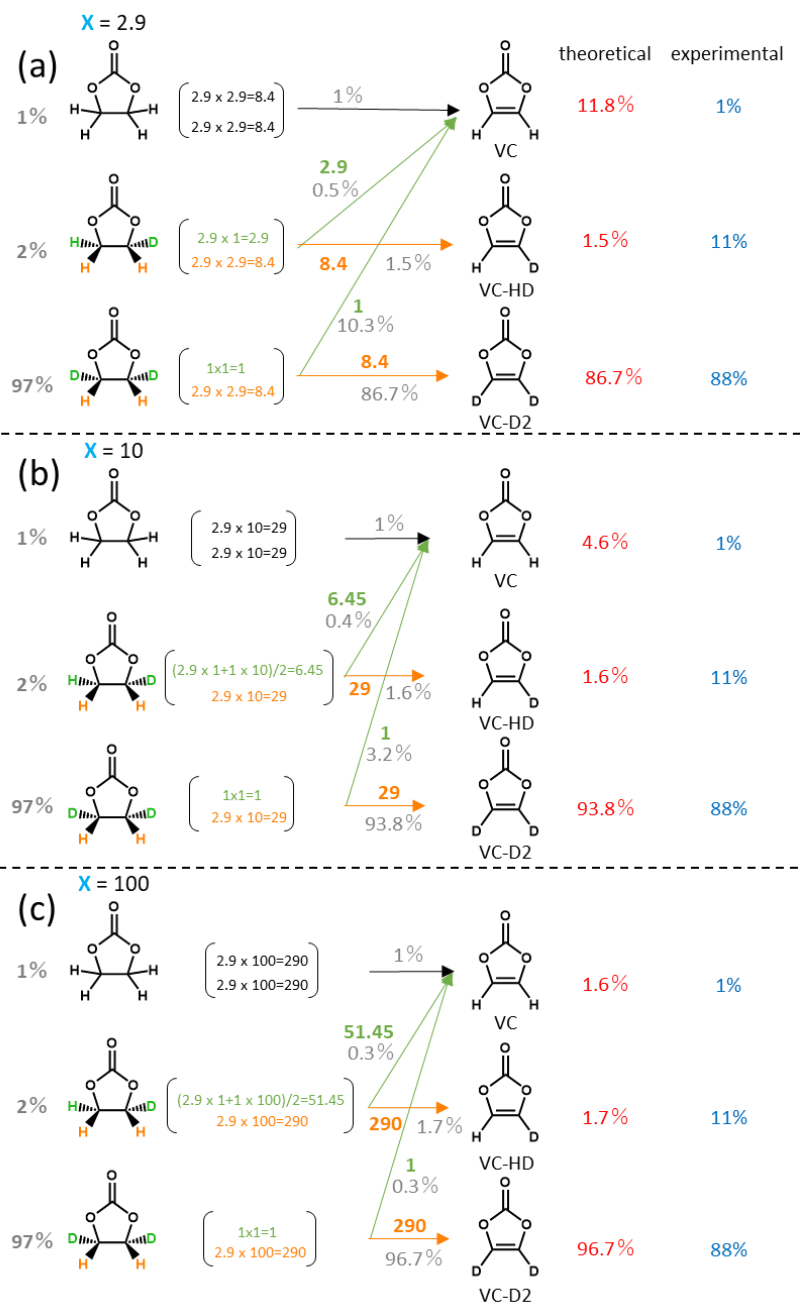


**Figure 7.** Proportions of isotopomers by simple calculations in VC-H<sub>2</sub>, VC-HD, and VC-D<sub>2</sub> generated from syn-EC-D<sub>2</sub> in the case of syn-elimination based on the kinetic isotope effect ( $k_H/k_D = 2.9$ ) in the first step and  $k_H/k_D = 2.9, 10,$  and  $100$  in the second step.

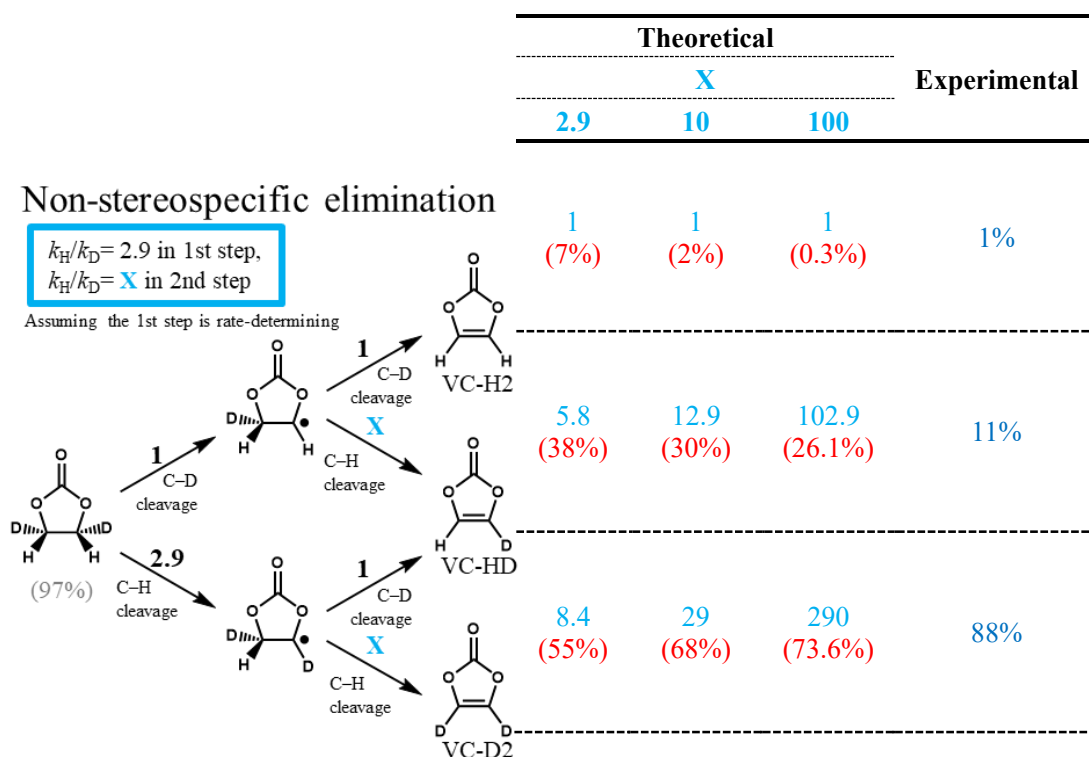


**Figure 8.** Proportions of isotopomers by simple calculations in VC-H2, VC-HD, and VC-D2 generated from syn-EC-D2 in the case of non-stereospecific elimination based on the kinetic isotope effect ( $k_H/k_D = 2.9$ ) in the first step and  $k_H/k_D = 2.9, 10,$  and  $100$  in the second step.

If a non-stereospecific reaction is assumed, the product ratios are shown in Figure 8. Again, the ratio of VC-D2 to VC-H2 is sufficiently high (73.6:0.3) when assuming  $k_H/k_D = 100$  in the second step. However, the ratio of VC-HD is  $>26.1\%$  regardless of the KIE value of the second step, which is much greater than the actual value of 11%. This discrepancy arises from the relatively large proportion ( $1/(1 + 2.9) = 26\%$ ) of the C–D bond cleaved intermediated generated from syn-EC-D2, although C–D bond cleaved products accounted for only 11% of the product. Consequently, three simple models, a one-step concerted mechanism, stereospecific two-step syn-elimination, and non-stereospecific reaction, cannot alone explain the proportions of the products formed. In reality, mechanisms, in which these mixes, are likely to occur. Still, it can be said that, overall, the syn-elimination process is the predominant mechanism.

Next, PC was used under the reaction conditions to examine the substrate generality of the reaction. The supposed product, methylvinylene carbonate, was synthesized according to a literature method (see the Supplementary Information for the detailed process) to determine whether the reaction was proceeding, even in small amounts. As a result, it was found that the hydrogen elimination reaction did not proceed in the presence of propylene carbonate at all. This result indicates that the oxidation reaction from EC to VC is unique, such that it is prevented by the steric hindrance of a methyl group. This is consistent with the fact that  $\Delta S^\ddagger$  has a large negative value and adopts a fixed transition state (Figure 9).

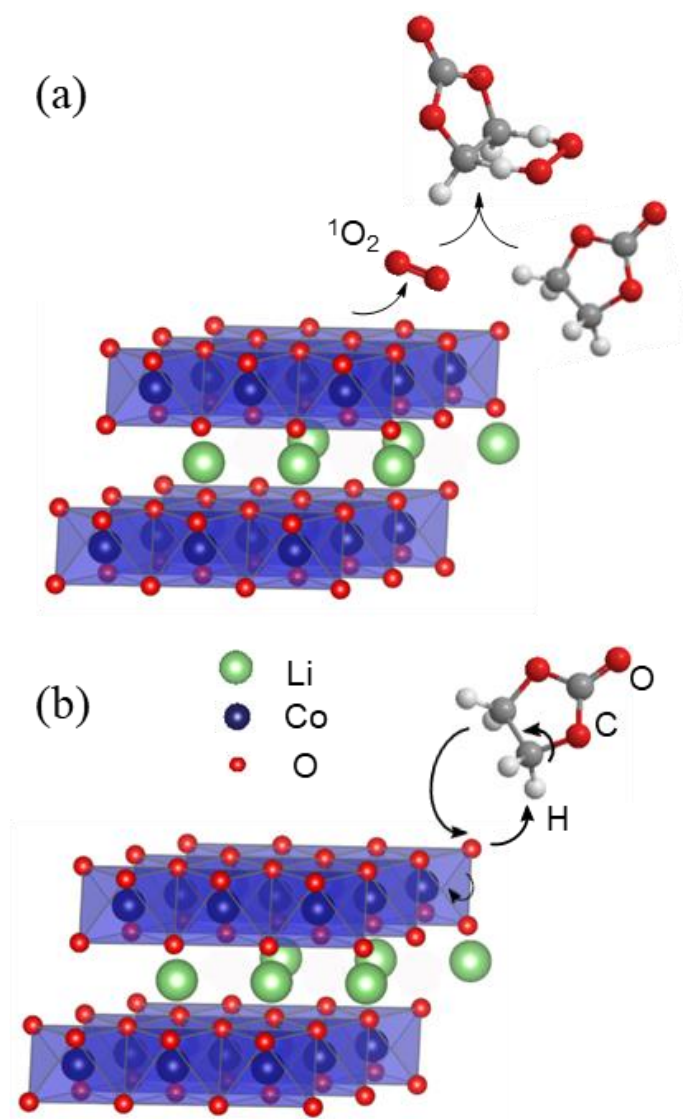


**Figure 9.** A possible reaction mechanism of EC (a) reacted with singlet oxygen to form a six-

membered ring [1.3] and (b) adsorbed on the  $\text{Li}_{1-x}\text{CoO}_2$ .

Shao-Horn et al. investigated the process of the cleavage of the C–H bonding of EC and its chemisorption on  $\text{Li}_{1-x}\text{CoO}_2$  using DFT calculations [1.7]. Although the steps that proceeded did not lead to VC formation in their study, the initial C–H activation may proceed via a similar mechanism. Additionally, for syn-stereospecific EC oxidation into VC by singlet oxygen, the  $\Delta G^\ddagger$  was 89–123  $\text{kJ mol}^{-1}$  was calculated by the DFT calculations [1.3], which is fairly close to the experimental results in this study (Table 2). The activation entropy ( $\Delta S^\ddagger$ ) should be a large negative value because the reaction adopts a rather fixed six-membered ring transition state. In the Diels–Alder reaction, which proceeds via a similar transition state,  $\Delta S^\ddagger$  is known to be negative ( $-201 \text{ J mol}^{-1} \text{ K}^{-1}$ ) [1.32]. In addition, a  $\Delta S^\ddagger$  of  $-313 \text{ J mol}^{-1} \text{ K}^{-1}$  has been reported in the transition state of an asymmetric Mannich reaction involving rigid multiple hydrogen bonding networks in [1.33].

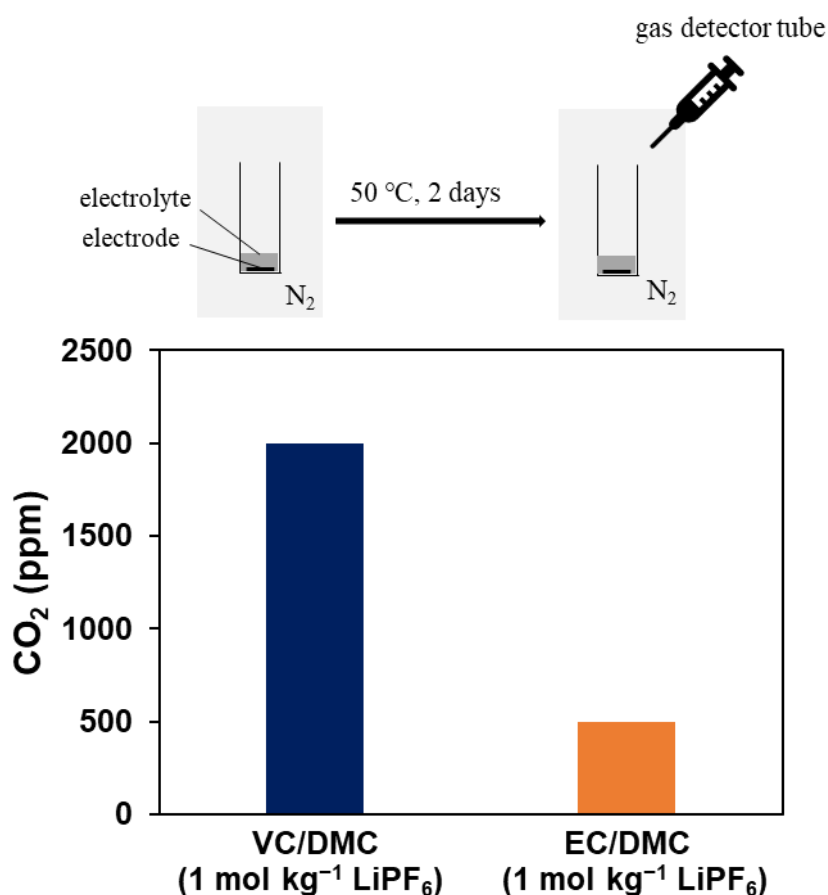


**Figure 10.** Amount of  $\text{CO}_2$  generated in each electrolyte (2 days after the reaction started).

At this stage, it is not possible to determine whether the mechanism proceeds via a reaction with singlet oxygen or C–H activation on the  $\text{Li}_{1-x}\text{CoO}_2$  surface, but neither can be ruled out. In the latter case, the hydrogen peroxide that is produced as a byproduct is difficult to detect as it is present in a very small amount and decomposes rapidly into water and oxygen. However, in both cases,  $\text{CO}_2$  was experimentally detected as the main byproduct, and in an independent experiment, a larger amount of  $\text{CO}_2$  was observed to be evolved from VC/DMC than from EC/DMC (Figure 10). As described by Freiberg et al., the decomposition of VC into  $\text{CO}_2$  is associated with a particularly low activation energy.

#### 2.4. Conclusion

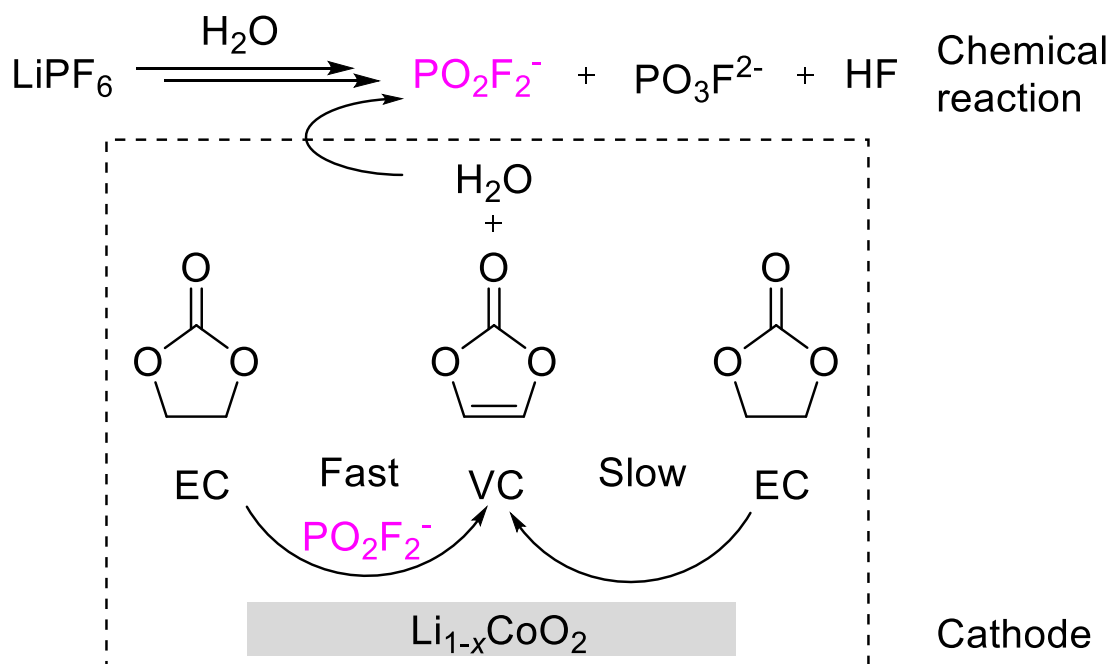


**Figure 11.** The overall scheme of electrochemical/chemical degradation processes described for EC/DMC (1:1 vol/vol) with  $\text{LiPF}_6$  ( $1 \text{ mol kg}^{-1}$ ) electrolyte.

The production of VC, that is one of the decomposition products of EC was observed in a mixed solvent of EC/DMC on charged  $\text{Li}_{1-x}\text{CoO}_2$  (4.5 V) in the presence or absence of  $\text{LiPF}_6$  (Figure 11). The mechanism of the formation of VC was investigated using KIEs, as well as Arrhenius and Eyring plots. VC was generated through a tied and orderly transition state involving irreversible C–H bond

cleavage from EC. Additionally, the elimination of hydrogens from EC proceeds mainly via syn stereochemistry (Table 2). Moreover, for the generation of VC, when  $\text{PO}_2\text{F}_2^-$ , which is one of the hydrolysis products of  $\text{LiPF}_6$ , was added, an accelerating effect was observed. In this study, the decomposition mechanism of electrolytes was analyzed under high voltage and the high temperature from both electro- and organic chemistry perspectives. The reaction of the formation of VC is accompanied by the generation of water, which then decomposes  $\text{LiPF}_6$  and carbonate esters. This is one of the important reactions in LIB degradation. It is thus hoped that this study provides a new perspective for future research on the development of safer LIBs and the design of more stable electrolyte components.

## 2.5. NMR Charts

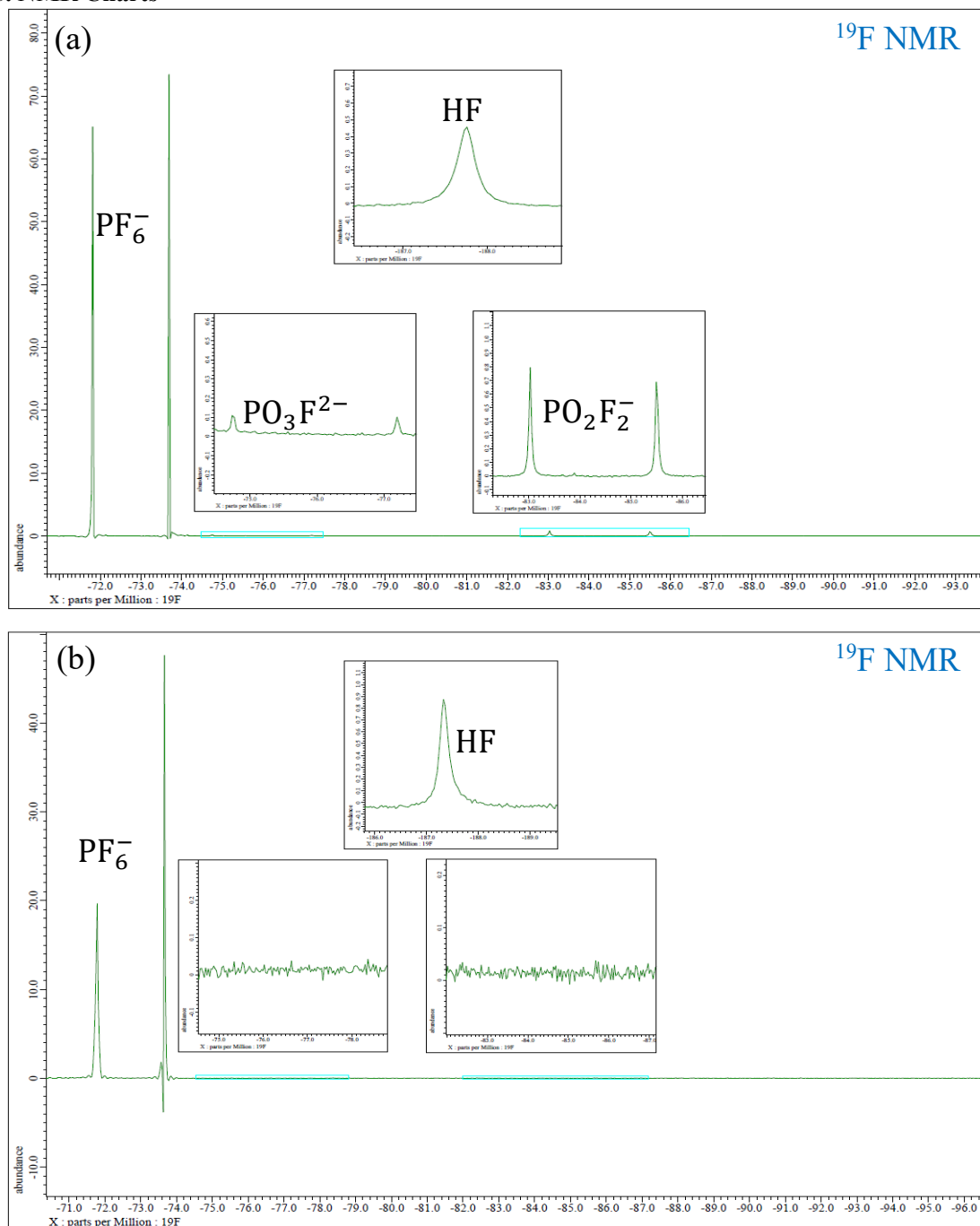


**Figure 12.**  $^{19}\text{F}$  NMR (376 MHz, acetone- $\text{D}_6$ ) charts of electrolyte containing  $\text{LiPF}_6$ .

(a) 4.5 V  $\text{LiCoO}_2$  electrode is not included.  $\text{PF}_6^-$  (-72.6 ppm, d,  $J = 705$  Hz, cf. -72.4 ppm, d,  $J = 708$  Hz [1.34]),  $\text{PO}_3\text{F}^{2-}$  (-76.0 ppm, d,  $J = 924$  Hz, cf. -76.7 ppm, d,  $J = 934$  Hz [1.34]), and  $\text{PO}_2\text{F}_2^-$  (-84.3 ppm, d,  $J = 925$  Hz, cf. -83.8 ppm, d,  $J = 975$  Hz [1.34]). (b) 4.5 V  $\text{LiCoO}_2$  electrode is included.  $\text{PF}_6^-$  (-72.7 ppm, d,  $J = 705$  Hz).



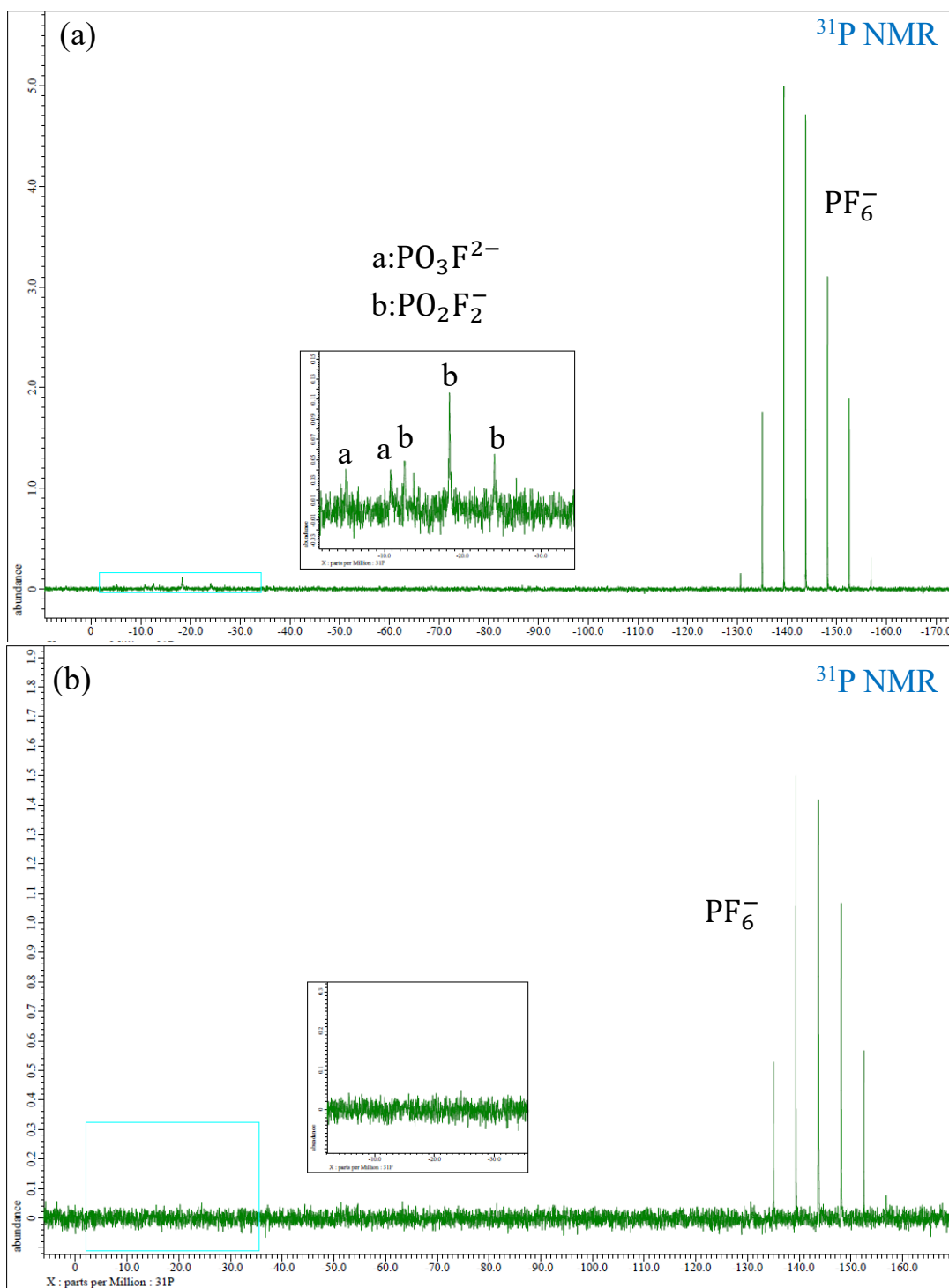


**Figure 13.**  $^{31}\text{P}$  NMR (162 MHz, acetone- $\text{D}_6$ ) charts of electrolyte containing  $\text{LiPF}_6$ . (a) 4.5 V  $\text{LiCoO}_2$  electrode is not included.  $\text{PF}_6^-$  (-143.7 ppm, sept,  $J = 707$  Hz, cf. -146.1 ppm, sept,  $J = 708$  Hz [1.34]),  $\text{PO}_2\text{F}_2^-$  and  $\text{PO}_3\text{F}^{2-}$  (Although it is difficult to see due to the noise, but the chemical shift and coupling constant of the peaks seems to be consistent with the literature [1.34]). (b) 4.5 V  $\text{LiCoO}_2$  electrode is included.  $\text{PF}_6^-$  (-143.7 ppm, sept,  $J = 707$  Hz).

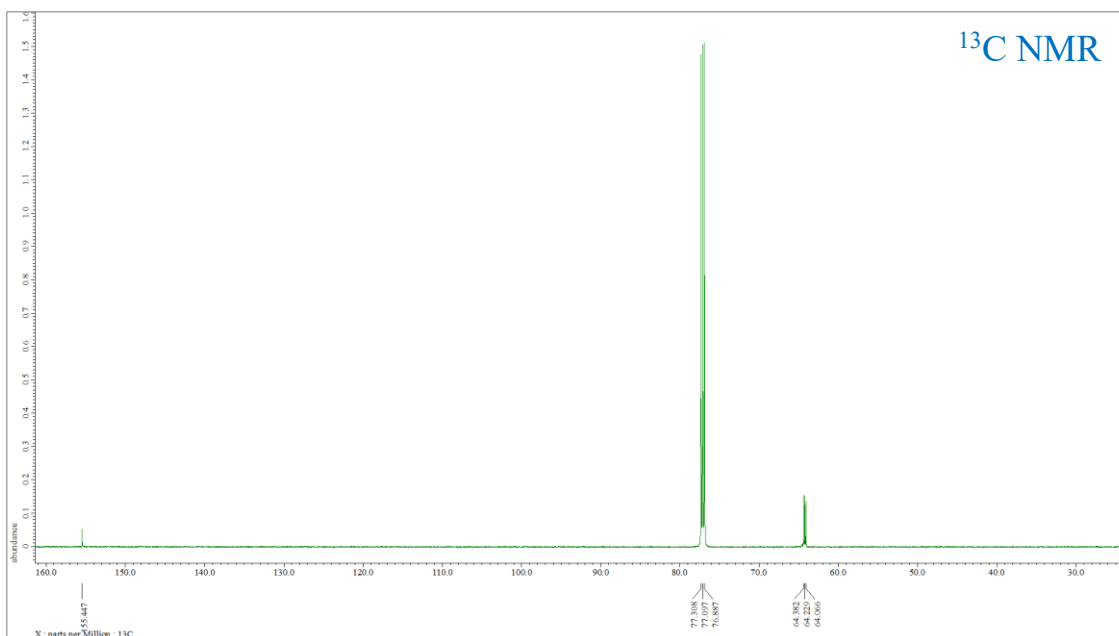
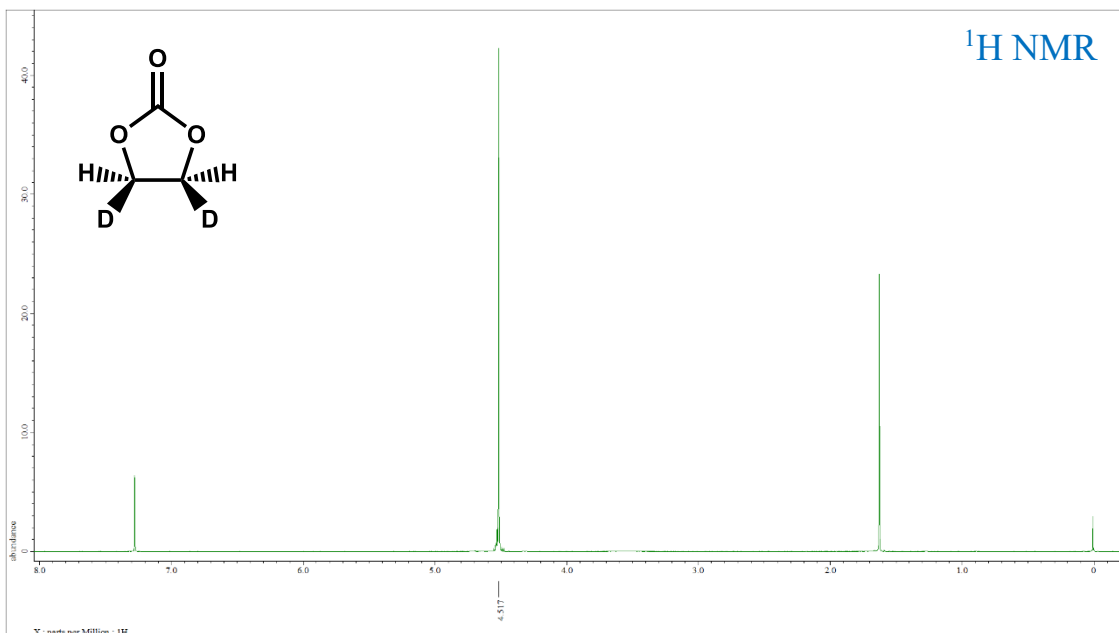


**Figure 14.** <sup>1</sup>H (600 MHz, CDCl<sub>3</sub>) and <sup>13</sup>C (150 MHz, CDCl<sub>3</sub>) NMR chart of EC-D2.

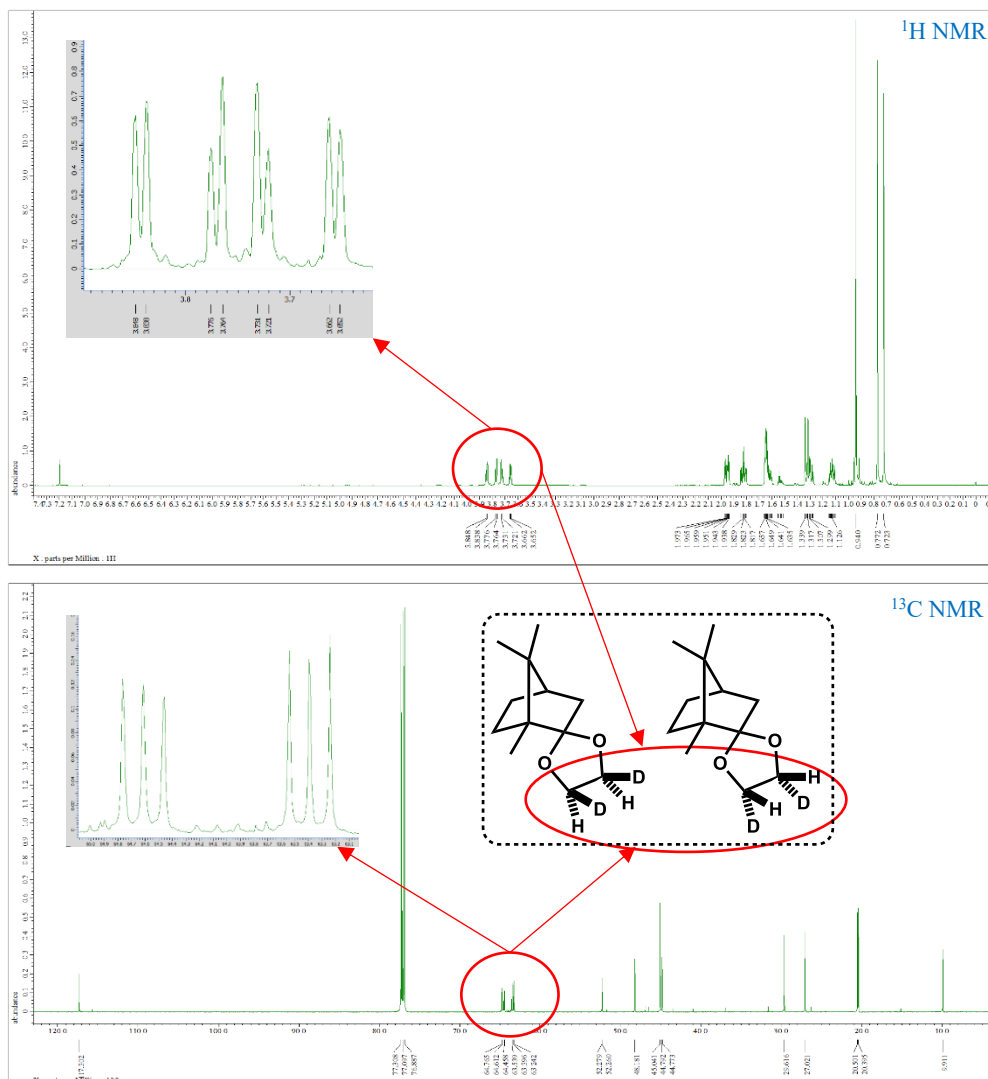


**Figure 15.**  $^1\text{H}$  (600 MHz,  $\text{CDCl}_3$ ) and  $^{13}\text{C}$  (150 MHz,  $\text{CDCl}_3$ ) NMR chart of 1,7,7-trimethylspiro[bicyclo[2.2.1]heptane-2,2'-[1,3]dioxolane] (D2).

As reported in the literature, the angle between the two vicinal hydrogens (H) in the acetal moiety can generally be determined from the coupling constant [1.35]. If the two H are in a relative configuration of syn, the coupling constants should be close for the produced two acetal-D2 molecules (Figure 15 (a)). On the other hand, if the two H are in the anti-relative configuration, the coupling constants are likely to be different (Figure 15 (b)).

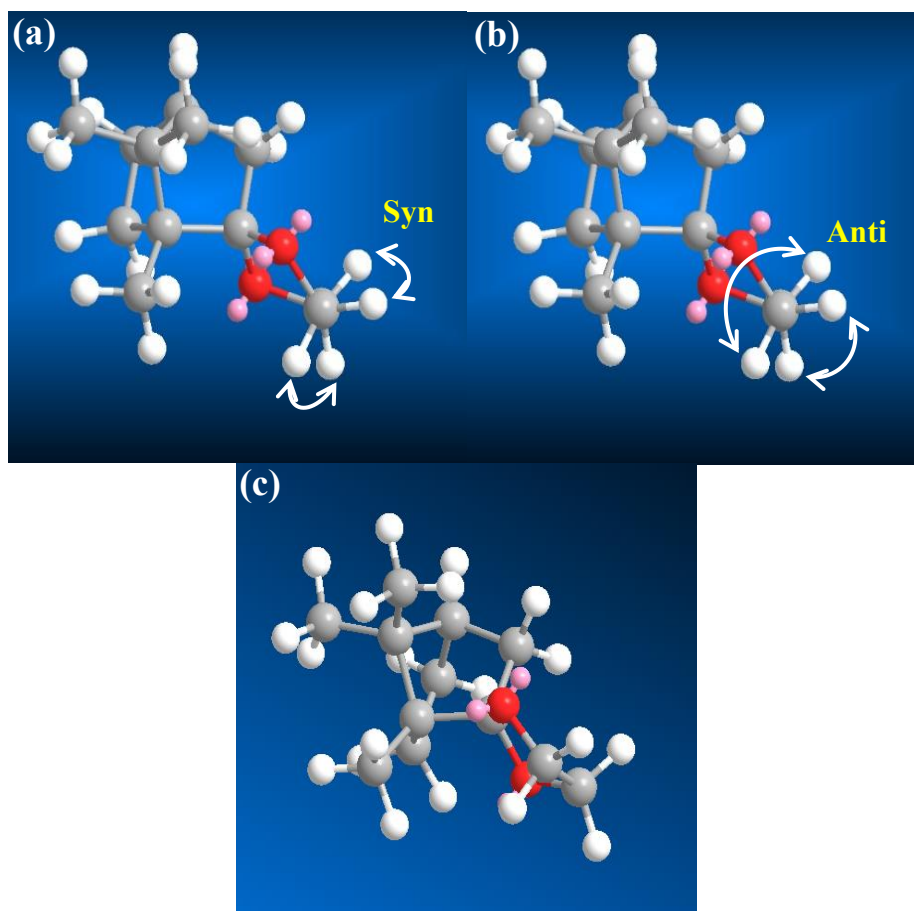


**Figure 16.** 1,7,7-trimethylspiro[bicyclo[2.2.1]heptane-2,2'-[1,3]dioxolane] (D2) from a Newman projection angle (a) syn, (b) anti, and (c) from a different direction.

## 2.6. References

- [2.1] Leung, K. *J. Phys. Chem. C* **2012**, *116*, 9852.
- [2.2] Venkatraman, S.; Shin, Y.; Manthiram, A. *Electrochem. Solid-State Lett.* **2003**, *6*, A9.
- [2.3] Freiberg, A. T.S.; Roos, M. K.; Wandt, J.; Vivie-Riedle, R.; Gasteiger, H. A. *J. Phys. Chem. A* **2018**, *122*, 8828.
- [2.4] Kong, L.; Li, C.; Jiang, J.; Pecht, M. G. *Energies* **2018**, *11*, 2191.
- [2.5] Xu, K. *Chem. Rev.* **2014**, *114*, 11503.
- [2.6] Borodin, O.; Ren, X.; Vatamanu, J.; Cresce, A. W.; Knap, J.; Xu, K. *Acc. Chem. Res.* **2017**, *50*, 2886.
- [2.7] Giordano, L.; Karayaylali, P.; Yu, Y.; Katayama, Y.; Maglia, F.; Lux, S.; Shao-Horn, Y. *J. Phys. Chem. Lett.* **2017**, *8*, 3881.
- [2.8] Tebbe, J. L.; Fuerst, T. F.; Musgrave, C. B. *ACS Appl. Mater. Interfaces* **2016**, *8*, 26664.
- [2.9] Rinkel, B. L. D.; Hall, D. S.; Temprano, I.; Grey, C. P. *J. Am. Chem. Soc.* **2020**, *142*, 15058.
- [2.10] Wandt, J.; Freiberg, A. T.S.; Ogrodnik, A.; Gasteiger, H. A. *Mater. Today* **2018**, *21*, 825.
- [2.11] Zhang, Y.; Katayama, Y.; Tatara, R.; Giordano, L.; Yu, Y.; Fraggedakis, D.; Sun, G. J.; Maglia, F.; Jung, R.; Bazant, M. Z.; Shao-Horn, Y. *Energy Environ. Sci.* **2020**, *13*, 183.
- [2.12] Späth, T.; Becker, D.; Schulz, N.; Hausbrand, R.; Jaegermann, W. *Adv. Mater. Interfaces* **2017**, *4*, 1700567.
- [2.13] Zhang, J.N.; Li, Q.; Wang, Y.; Zheng, J.; Yu, X.; Li, H. *Energy Stor. Mater.* **2018**, *14*, 1-7.
- [2.14] Buchner, F.; Fingerle, M.; Kim, J.; Späth, T.; Hausbrand, R.; Behm, R. *J. Adv. Mater. Interfaces* **2019**, *6*, 1801650.
- [2.15] Leißing, M.; Peschel, C.; Horsthemke, F.; Wiemers-Meyer, S.; Winter, M.; Nowak, S. *Batteries Supercaps* **2021**, *4*, 1731.
- [2.16] Bigovic, M.; Maslak, V.; Tokic-Vujosevic, Z.; Divjakovic, V.; Saicic, R.N. *Org. Lett.* **2011**, *13*, 4720.
- [2.17] Osborn, J. A.; Jardine, F. H.; Young, J. F.; Wilkinson, G. *J. Chem. Soc. A* **1966**, 1711.
- [2.18] Li, T.; Xing, L.; Li, W.; Wang, Y.; Xu, M.; Gu, F.; Hu, S. *J. Power Sources* **2013**, *244*, 668.
- [2.19] Plakhotnyk, A. V.; Ernst, L.; Schmutzler, R. *J. Fluor. Chem.* **2005**, *126*, 27.
- [2.20] Lei, Q.; Yang, T.; Zhao, X.; Fan, W.; Wang, W.; Yu, L.; Guo, S.; Zuo, X.; Zeng, R.; Nan, J.

- J. Electroanal. Chem.* **2019**, *846*, 113141.
- [2.21] Takiguchi, M.; Ichikawa, S. *Jpn. Kokai Tokkyo Koho* (**1999**), publication No. JP 1999-171882.
- [2.22] Newman, M. S.; Addor, R. W. *J. Am. Chem. Soc.* **1955**, *77*, 3789.
- [2.23] Johnson, W. K.; Patton, T. L. *J. Org. Chem.* **1960**, *25*, 1042.
- [2.24] Simmons, E. M.; Hartwig, J. F. *Angew. Chem. Int. Ed.* **2012**, *51*, 3066.
- [2.25] Osborn, J. A.; Jardine, F. H.; Young, J. F.; Wilkinson, G. *J. Chem. Soc. A* **1966**, 1711.
- [2.26] Kalyani, D.; Marlier, E. E. Chapter 24 in *Arene Chemistry: Reaction Mechanisms and Methods for Aromatic Compounds*. 1st Ed. Mortier, J. Ed. *John Wiley & Sons, Inc.*, Hoboken, New Jersey **2016**.
- [2.27] García-Cuadrado, D.; Braga, A. A. C.; Maseras, F.; Echavarren, A. M. *J. Am. Chem. Soc.* **2006**, *128*, 1066.
- [2.28] Tran, B. L.; Driess, M.; Hartwig, J. F. *J. Am. Chem. Soc.* **2014**, *136*, 17292.
- [2.29] Man, W.L.; Lam, W. W. Y.; Kwong, H.K.; Yiu, S.M.; Lau, T.C. *Angew. Chem. Int. Ed.* **2012**, *51*, 9101.
- [2.30] Kamijo, S.; Takao, G.; Kamijo, K.; Hirota, M.; Tao, K.; Murafoji, T. *Angew. Chem. Int. Ed.* **2016**, *55*, 9695.
- [2.31] Matsumoto, T.; Ohkubo, K.; Honda, K.; Yazawa, A.; Furutachi, H.; Fujinami, S.; Fukuzumi, S.; Suzuki, M. *J. Am. Chem. Soc.* **2009**, *131*, 9258.
- [2.32] Jorgensen, W. L.; Lim, D.; Blake, J. F. *J. Am. Chem. Soc.* **1993**, *115*, 2936.
- [2.33] Han, X.; Lee, R.; Chen, T.; Luo, J.; Lu, Y.; Huang, K.W. *Sci. Rep.* **2013**, *3*, 2557.
- [2.34] Plakhotnyk, A. V.; Ernst, L.; Schmutzler, R. *J. Fluor. Chem.* **2005**, *126*, 27.
- [2.35] Karplus, M. *J. Am. Chem. Soc.* **1963**, *85*, 2870.

## **Chapter 3. Liquid Phase Oxidation of Methacrolein into Methacrylic Acid with Supported Au Catalysts**

### **3.1. Introduction**

Methacrylic acid (MAA) is an industrially important compound for the production of methyl methacrylate (MMA). It is traditionally produced from a process of acetone cyanohydrin (ACH) using toxic formonitrile and corrosive  $\text{H}_2\text{SO}_4$ , and this process could cause a negative impact on the environment. It also can be produced from the oxidation of methacrolein (MAL) to MAA in an environmentally friendly process [3.1–3.5], which is one of the well-researched sustainable production processes of MMA. In this process, heteropolyacids and polyoxometalates, are usually used as catalysts owing to their easily adjustable acidity and redox properties. [3.6, 3.7] However, the heteropoly compounds used as catalysts usually need higher reaction temperatures and lead to higher costs because of their poor thermal stability. Therefore, it is necessary to find a new catalyst to avoid these deficiencies.

A variety of catalysts have been developed for the oxidation of aldehydes to carboxylic acids, including metal-free catalysts, such as activated carbon [3.8, 3.9] and  $\beta$ -cyclodextrin [3.10], and catalysts containing metal elements of gold (Au) [3.11], iron (Fe) [3.12], selenium (Se) [3.13], palladium (Pd) [3.14–3.16] respectively. In particular, Au nanostructured catalysts have been perhaps the most widely researched in the last few years, owing to their potential applicability to various reactions with the consideration of economic and environmental benefits [3.17, 3.18]. Especially for partial or full oxidation, are diverse. It has been observed that bulk Au is the least active among the noble metals group, but when it is highly dispersed on a reducible metal support such as  $\text{TiO}_2$ , Au exhibits surprisingly high activity for CO oxidation at low temperatures [3.19], and it has also shown activity for methanol oxidation [3.20]. However, the catalytic performance of Au-based catalytic systems can be highly affected by the preparation method and the type of support. Various metal oxides such as  $\text{TiO}_2$  [3.21],  $\text{CeO}_2$  [3.22],  $\text{ZrO}_2$  [3.23],  $\text{MgO}$  [3.24], and  $\text{SiO}_2$  [3.25] are often used in oxidation reactions as support for Au. Due to the different physicochemical properties, Au catalysts on different supports could exhibit different activities for the same reactant. For example, the shape of the exposed Au may change with different metal-support interactions. For low-temperature CO oxidation, Grunwaldt et al. achieved only 15% CO conversion for the Au/ $\text{ZrO}_2$  catalyst, but 100% for Au/ $\text{TiO}_2$ .

It was contributed by the change in CO adsorption capacity due to the difference in the crystallinity of Au supported on different metal oxides [3.26]. In fact, many studies stated the importance of the preparation conditions in determining the morphology of the Au nanoparticles and the type of metal-support interactions [3.27, 3.28], both are able to profoundly modify the activity and/or the selectivity of the catalyst; Nevertheless, it is noticeable that for the oxidation reaction of methacrolein, there are plenty of researches based on heteropoly acid catalysts whereas the studies on Au nano-particles catalyst was so limited [3.29, 3.30], probably because of the lower activity compared with the heteropoly acid catalysts.

As a way, bimetallic catalyst systems have been used to improve the activity, selectivity and stability, compared to their monometallic catalyst [3.31, 3.32]. It is known that the physical and chemical properties of bimetallic particles are different from those of the monometallic ones, including changes in their optical and electronic properties, which are adjustable with metal specie and particle size. For instance, based on the oxidation reaction of *n*-octanol, Pestryakov et al. investigated the electronic state of Au by loading Fe and magnesium oxides to Au/TiO<sub>2</sub>, respectively. Au in a reduced state is found in the presence of magnesium oxide, which has the ability to donate electrons, while Au in an oxidized state is shown in the case of Fe oxide, which has the ability to accept electrons. As a result, it was reported that the more reduced Au is advantageous for *n*-octanol oxidation reaction [3.33]. Therefore, the final composition of these catalysts depends strongly on the method of preparation, the interaction between metals, the atmosphere and temperature of activation, etc. There was a great enhancement of catalytic properties in many reactions when combining Au with other metals to form new active sites induced by synergistic effects [3.34].

Based on the above discussion, in this work, various catalysts which ranging from Au monometallic catalysts to Au bimetallic catalysts were explored. Particle size and physicochemical properties of the catalyst were investigated by MP-AES, TEM, H<sub>2</sub>-TPR and XPS analysis. MAL conversion and MAA yield were examined GC. Using various measurement results, factors that promote the MAL selective oxidation reaction were proposed and the cause of this was investigated.



## 3.2. Experimental

### 3.2.1 Chemicals and Materials

HAuCl<sub>4</sub>·4H<sub>2</sub>O was purchased from Tanaka Kikinzoku Kogyo K.K. Ca(NO<sub>3</sub>)<sub>2</sub>·4H<sub>2</sub>O, Mg(NO<sub>3</sub>)<sub>2</sub>·6H<sub>2</sub>O, Ba(NO<sub>3</sub>)<sub>2</sub>, Fe(NO<sub>3</sub>)<sub>3</sub>·9H<sub>2</sub>O, 1,4-Dioxane, pyridine and heptane were purchased from FUJIFILM Wako Pure Chemical Corporation. Re<sub>2</sub>O<sub>7</sub>, Ca(OH)<sub>2</sub> and triethylamine (TEA) was purchased from Sigma-Aldrich Co. LLC. Mn(OAc)<sub>2</sub>·nH<sub>2</sub>O (Mn was measured to be about 16 weight% by MP-AES), La(NO<sub>3</sub>)<sub>3</sub>·6H<sub>2</sub>O were purchased from Wako Pure Chemical Industries, Ltd. Zn(OAc)<sub>2</sub>·2H<sub>2</sub>O, Cu(NO<sub>3</sub>)<sub>2</sub>·3H<sub>2</sub>O, Pr(NO<sub>3</sub>)<sub>3</sub>·6H<sub>2</sub>O were purchased from Kanto Chemical CO., Inc. Ni(OAc)<sub>2</sub>·2H<sub>2</sub>O were purchased from Kishida Chemical Co., Ltd. Cr<sub>2</sub>O<sub>3</sub> was purchased from NACALAI TESQUE, INC. ZrO<sub>2</sub> (JRC-ZRO-4), CeO<sub>2</sub> (JRC-CEO-3, 81 m<sup>2</sup>/g), Al<sub>2</sub>O<sub>3</sub> (JRC-ALO-9) and TiO<sub>2</sub> (JRC-TIO-4, JRC-TIO-15) were obtained from the Catalysis Society of Japan. MgO (8 m<sup>2</sup>/g) was purchased from Ube Industries, Ltd. TiO<sub>2</sub> (ST-01) was obtained from ISHIHARA SANGYO KAISHA, LTD. TiO<sub>2</sub> (100N) was obtained from SAKAI CHEMICAL INDUSTRY CO., LTD.

### 3.2.2 Preparation of Catalyst

#### 3.2.2.1 Preparation of Monometallic Samples

TiO<sub>2</sub> was used as support (50±15 m<sup>2</sup> g<sup>-1</sup>, about 80% anatase and 20% rutile, purity >99.5%). Commercial HAuCl<sub>4</sub>·4H<sub>2</sub>O and Mn(OAc)<sub>2</sub>·nH<sub>2</sub>O were used as Au and Mn precursors. The nominal metal loadings in the monometallic catalysts were 1 wt.% for Au and 0.6 wt.% for Mn.

The preparation of the Au/TiO<sub>2</sub> sample was performed by deposition-precipitation (DP) method with ammonium carbonate at room temperature, according to the previously reported procedure.<sup>5</sup> In this preparation, the TiO<sub>2</sub> support (1 g) and ammonium carbonate (2.5 g) were dispersed in 80 mL of distilled water, and stirred for 15 minutes. Then, HAuCl<sub>4</sub>·4H<sub>2</sub>O aqueous solution (25 mg, 20 mL) was dropped to this solution. The suspension kept constant for 4 h under vigorous stirring at room temperature. Afterwards, the suspension was filtered, washed with water (100 mL) two times and hot water (100 mL) one time. The solid recovered was dried under vacuum for 4 h at 50°C and calcined at 300°C for 0.5 h in air, labeled as 1wt%Au/TiO<sub>2</sub>.

The monometallic Mn/TiO<sub>2</sub> sample was prepared by impregnation (IP) method. 1 g of TiO<sub>2</sub> support was added to an aqueous solution (1 mL) containing Mn(OAc)<sub>2</sub>·nH<sub>2</sub>O (37.5 mg) in a mortar and

churned for 30 min. The slurry was dried under vacuum for 4 h at 50°C and calcined at 300°C for 0.5 h in air, labeled as 0.6wt%Mn/TiO<sub>2</sub>.

### 3.2.2.2 Preparation of Bimetallic Samples

In bimetallic samples, the nominal Au loading was kept constant (1 wt.%), whereas for manganese was chosen to synthesize Au-Mn catalysts with different Au: Mn weight ratios: 1:0.2, 1:0.4, 1:0.6, 1:0.8, 1:1, 1:2, 1:4 and 1:12. DP and IP method was used continuously to prepare these catalysts. Au was first deposited on TiO<sub>2</sub>, according to the DP method described above. After being dried at 50°C for 4 h (do not calcine), then manganese was supported by IP as previously described. The samples were calcined at 300°C for 0.5 h in air, labeled as 1wt%Au-*x*wt%Mn/TiO<sub>2</sub>.

In addition, 1wt%Au-*x*%M/TiO<sub>2</sub> (M = Mg, Ca, Ba, Re, Zn, Ni, Cu, Cr, Fe, La and Pr) catalysts were also prepared by the same preparation method. where *x* is the manganese content in wt.%,

### 3.2.3 Characterization Techniques

The amount of methacrolein and methacrylic acid were analyzed by GC (Agilent GC 6850 Series II equipped with FID), which is equipped with a J&W HP-INNOWAX column (0.25 μm thickness, 0.25 mm I.D., 30 m).

The elemental analysis of Au and Mn in the dried samples was performed by microwave plasma atomic emission spectrometer (MP-AES) using an Agilent 4100 system.

The samples were examined by scanning transmission electron microscopy (STEM) in a JEOL JEM-ARM200F analytical microscope equipped with a bright-field (BF) detector. The average size of particles and the histograms of particle sizes were obtained from the measurement of 176–295 particles. It also offers a highly efficient dual EDS system with a collection solid angle close to 2 sr. The STEM-EDS maps, line scan profiles and compositions were collected using the AnalysisStation software.

X-ray powder diffraction (XRD) was conducted by the Rigaku MiniFlex600 with a CuK $\alpha$  radiation.

X-ray photoelectron spectroscopy (XPS) analyses were performed on a Shimadzu-AXIS-165 spectrometer equipment in The Ultramicroscopy Research Center of Kyushu University with an Al K $\alpha$  radiation source at a pressure below 10<sup>-8</sup> Pa. The binding energy (BE) scale was calibrated to the peak at 284.8 eV of adventitious carbon. The fitting analysis was performed using XPSPEAK41 software.

Temperature-programmed reduction of H<sub>2</sub> (H<sub>2</sub>-TPR) experiments were carried out using a BELCAT instrument equipped with a thermal conductivity detector (TCD). A gas mixture of 5 % H<sub>2</sub> in Ar with flow rate of 20 mL/min was flown through samples (100 mg). The heating rate was 10 °C/min. To prevent the influence of water vapor on TCD-signal, a desiccant trap with a molecular sieve 3A was used.

### 3.2.4 Catalytic Activity

The performance of the oxidation of methacrolein was evaluated using an autoclave (40 mL). For each experiment, 160 mg of powder catalyst, solution (2.9 mL) of *tert*-Butyl Alcohol (*t*-BuOH)/ H<sub>2</sub>O and methacrolein (2 mmol) was added in the autoclave, then fill with air to 1 MPa. The reaction mixture was stirred in the autoclave for 4 h at 100 °C, and the reaction conditions were referred to the reported literature [3.29].

In addition, the reaction mixture was also stirred in the autoclave with the amount of catalyst (480 mg) and solution (2.9 mL) of *t*-BuOH/ H<sub>2</sub>O under the 24h-reaction temperature of 50°C to increase MAA selectivity.

### 3.2.5 Precipitate Polymers of MAL and MAA which are By-products

A solution (*t*-BuOH/H<sub>2</sub>O) containing MAL (2 mmol) was heated in a flask at 100°C for 4 hours without a catalyst. Then after evaporating more than half of the residual liquid with a vacuum evaporator, added a large amount of dimethyl ether to precipitate the polymers of MAL.

For MAA, 1wt%Au-0.6wt%Mn/TiO<sub>2</sub> was added to a solution containing MAA (2 mmol) and heated in the flask under the same conditions. Afterwards, the suspension was centrifuged to remove the catalyst. Then after evaporating more than half of the residual liquid with a vacuum evaporator, added a large amount of dimethyl ether to precipitate the polymers of MAA.

### 3.3. Results and Discussion

#### 3.3.1 Searching for Optimal Catalyst and Catalytic Performance

##### 3.3.1.1 Optimizing Supported Au Catalyst and Reaction Time

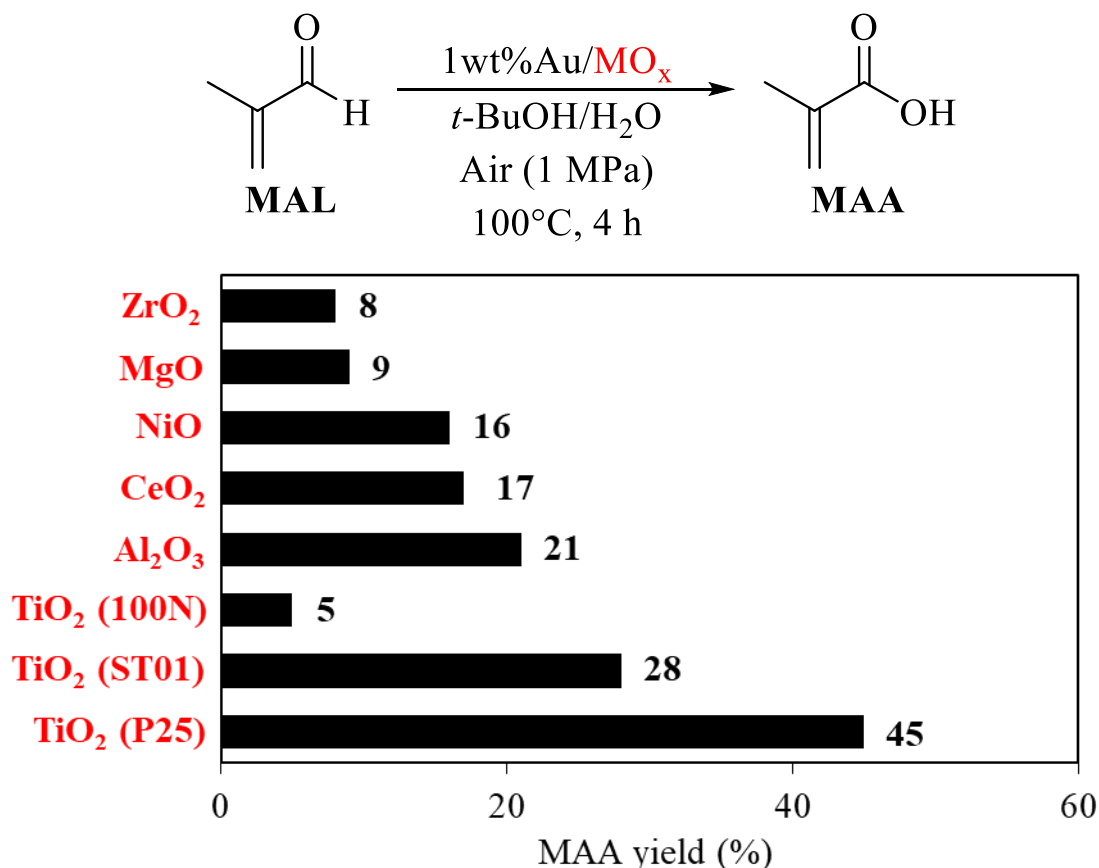


**Figure 1.** Investigation of MAA yield in methacrolein oxidation reaction with different supports of Au-supported catalyst.

Figure 1 shows the yield of methacrylic acid in methacrolein oxidation reaction with different supports of Au-supported catalysts (transition metal and non-transition metal). All catalysts were prepared by deposition precipitation (DP). For transition metal oxide, there is a special oxide surface called oxygen vacancies. Besides, it is often used in heterogeneous catalysts. TiO<sub>2</sub> and ZrO<sub>2</sub> are used as catalyst support for various oxidation reactions such as carbon monoxide (CO) [3.34, 3.35] and alcohol oxidation [3.32] reaction. However, in this study, much higher catalytic activity was observed for catalysts with Au supported on TiO<sub>2</sub> than ZrO<sub>2</sub>. The mechanism of MAL oxidation reaction is still not clearly understood, but it is probably related to O<sub>2</sub> adsorption capacity. It has been reported that Au-supported titania catalyst has better O<sub>2</sub> adsorption capacity than Au-supported zirconia catalyst in

CO oxidation [3.26]. One of the reasons is considered to be the change of Au charge state. Most of negatively charged  $\text{Au}^{\sigma^-}$  exists on  $\text{TiO}_2$  [3.32]. In the contrary,  $\text{Au}^0$  mainly exists on  $\text{CeO}_2$  [3.36]. In addition, through the investigation of titania with different crystal structures, the best catalytic activity was found in the catalyst that Au is supported on P25 (anatase/ rutile, 8/ 2), and the MAA yield was 45%. Davis et al. investigated the mechanism of alcohol oxidation by DFT calculation and reported that carboxylic acid is easily generated in Au-supported  $\text{TiO}_2$  catalysts. It is proposed that hydroxide ions abundantly present on the metal surface contribute to the catalytic cycle [3.37]. Compared to transition metals oxide, the catalytic activities of catalysts with non-transition metals were lower. Especially, the highest MAA yield was found for  $\text{Al}_2\text{O}_3$  with 21%, which was about twice lower than that of  $\text{TiO}_2$  (P25). Nevertheless, for MAA yield of  $\text{MgO}$ , it is even less than 10%.

**Table 1.** Investigation of reaction time, amount of Au loading, and effect of support.

$\text{MAL} \xrightarrow[\text{Air (1 MPa), 100 }^\circ\text{C}]{\text{Catalyst, } t\text{-BuOH/H}_2\text{O}} \text{MAA}$

Entry	Catalyst	Time (h)	MAL Conv. (%) <sup>a</sup>	MAA Selec. (%) <sup>a</sup>
1	1 wt% Au/ $\text{TiO}_2$	4	58	78
2	1 wt% Au/ $\text{TiO}_2$	12	78	67
3	1 wt% Au/ $\text{TiO}_2$	18	81	81
4	1 wt% Au/ $\text{TiO}_2$	24	98	77
5	none	4	52	13
6 <sup>b</sup>	$\text{TiO}_2$ (P25)	4	19	21

Reaction conditions: Au/ $\text{TiO}_2$  (0.4 mol%,  $\text{TiO}_2$ : P25), MAL (2 mmol), *t*-BuOH (1.2 mL),  $\text{H}_2\text{O}$  (1.7 mL) in 40 mL autoclave. <sup>a</sup>GC analyses.

<sup>b</sup> $\text{TiO}_2$  (160 mg) was used.

For Au/ $\text{TiO}_2$ , the reaction time, loading amount and effect of support were investigated (Table 1). MAL conversion gradually increased to 98% with little change in MAA selectivity when the reaction time increased from 4 h to 12 h, 18 h and 24 h (entries 1–4). To clarify the interaction between Au and the support in the MAL oxidation reaction, the reaction without a catalyst and with the support of  $\text{TiO}_2$  was investigated (entries 5, 6). As a result, less than 20% of the substrate was consumed when support  $\text{TiO}_2$  was added as a catalyst, while more than half of the substrate was consumed when there was no catalyst. In addition, it was confirmed that the contribution of support  $\text{TiO}_2$  to the catalytic activity was small due to the lower yield of MAA. However, in the reaction without a catalyst, more than half

of the substrate was consumed. Besides, the substrate of methacrolein which is a kind of unsaturated aldehyde is so light, unstable and readily polymerizes that it is possible the large substrate decomposition and polymer formation.

### 3.3.1.2 Confirmation of Base Additive Effect

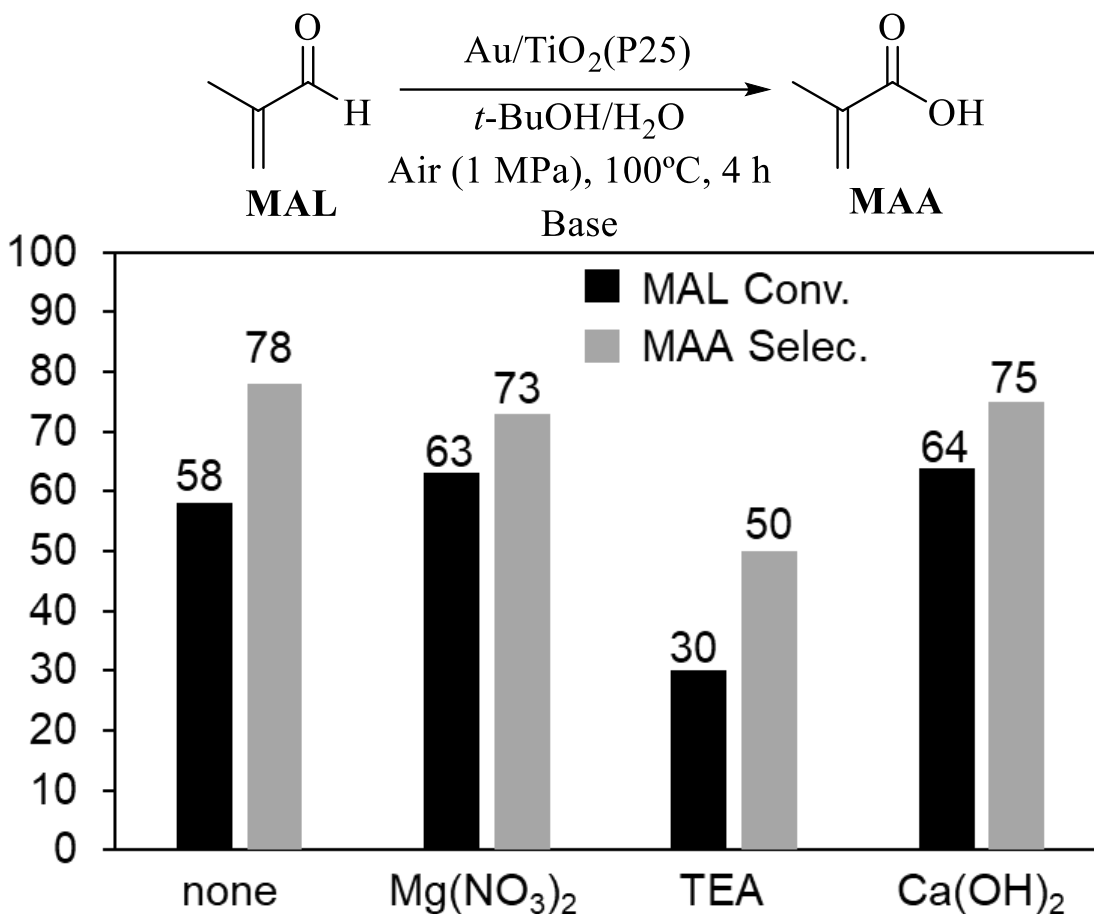


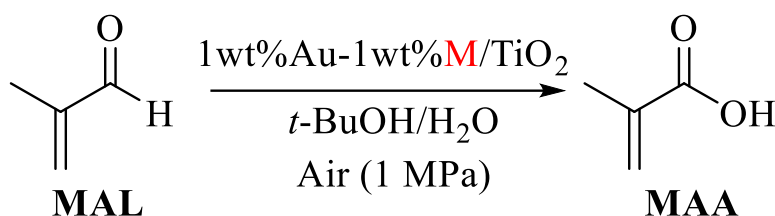
**Figure 2.** Addition effect of various base additives on methacrolein oxidation reaction

It was reported that basic additives are often used to facilitate the oxidation reaction of aldehydes [3.38]. Therefore, the reaction performances with small additions of three different types of bases were investigated by comparing the MAA yield (Figure 2). It was found that the reaction performance deteriorated with the addition of strong organic base triethylamine (TEA). In addition, even if a small amount of inorganic base (Mg(NO<sub>3</sub>)<sub>2</sub> and Ca(OH)<sub>2</sub>) was added, there was little change in the yield of MAA was observed, indicating that free base ions were not effective in promoting the reaction.

However, although it seems that adding a large amount of base may cause a positive effect, the carboxylic acid salt generated during the reaction should be neutralized with a stronger acid, then caused a large amount of inorganic sulfide by-products. It is not economically viable. Therefore, in order to avoid the addition of base, a bimetallic nanoparticle catalyst that can achieve high activity and high selectivity than simple Au-supported catalyst are considered to be a promising research direction.

### 3.3.1.3 Examination of Alkaline Earth Metals as Secondary Metals

**Table 2.** Effect of Addition of Alkaline Earth Metal as Second Metal and Investigation of Reaction Conditions



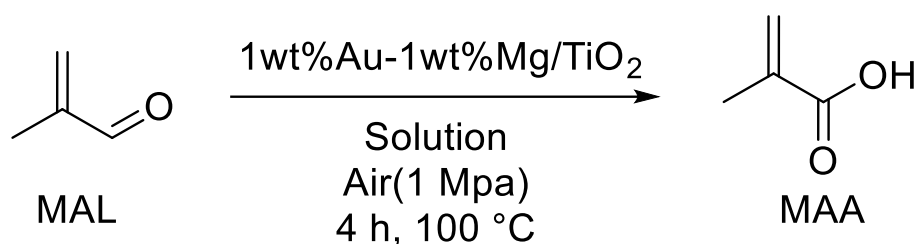
Entry	M	Au (mol%) <sup>a</sup>	Time (h)	Temp. (°C)	Conv. (%) <sup>b</sup>	Selec. (%)
1	none	0.4	4	100	58	78
2	Mg	0.4	4	100	72	80
3	Ca	0.4	4	100	73	75
4	Ba	0.4	4	100	77	80
5	Mg	0.4	14	90	91	80
6	Mg	0.4	24	80	96	79
7	Mg	0.4	24	60	79	85
8	Mg	0.9	24	50	88	85
9	Mg	1.3	24	50	98	84

Reaction conditions: substrate (2 mmol), *t*-BuOH (1.2 mL), H<sub>2</sub>O (1.7 mL) in 40 mL autoclave. <sup>a</sup> MP-AES analyses. <sup>b</sup> GC analyses.

Bimetal-supported catalysts containing Au and basic alkaline earth oxides were examined with the consideration of catalyst amounts, reaction times and temperatures as shown in Table 2. When three kinds of alkaline earth metals (Mg, Ca, Ba, all 1 wt%) were added as secondary metals to Au/TiO<sub>2</sub>, A kinetic enhancement effect was observed as MAL conversion was increased by 14–19% (Entries 1–

4). This is probably due to the change in the surface state of Au upon the addition of Mg oxide [3.32]. However, since the MAA selectivity was not improved, the ways of reduction by-product were investigated. To prevent substrate polymerization which is one of the factors related to by-products, the reaction performance was evaluated at lower temperatures. MAA selectivity did not change even when the reaction temperature was lowered to 80°C, but improved selectivity was observed at 60–50°C. However, when the reaction temperature was 50°C, the reaction was not finished even after 24 hours, therefore the amount of catalyst was examined. As a result, selectivity of MAA and conversion of MAL up to 84% and 98% were obtained when reacting for 24 hours at 50°C using 1wt%Au-1wt%Mg/TiO<sub>2</sub> catalyst (about 1.2 mol% Au). However, the elemental content of the catalyst after the reaction was measured and almost of Mg (> 90%) was leached. The reason could be that the form of hydroxide for Mg under the calcined condition of 300°C in air. This hydroxide for Mg could be solved in the acidic solution caused by the production of MAA. As a result, the leaching of Mg might have occurred.

**Table 3.** Investigation of Reaction Solvent Effect



Entry	Solution	Ratio (mL / mL)	Conv. (%) <sup>a</sup>	Selec. (%)
1	<i>tert</i> -Butyl alcohol / H <sub>2</sub> O	2.6 / 0.4	47	85
2	<i>tert</i> -Butyl alcohol / H <sub>2</sub> O	2.2 / 0.8	54	80
3	<i>tert</i> -Butyl alcohol / H <sub>2</sub> O	1.8 / 1.2	61	80
4	<i>tert</i> -Butyl alcohol / H <sub>2</sub> O	1.2 / 1.7	70	76
5	Heptane / H <sub>2</sub> O	1.2 / 1.7	74	57
6	1,4-Dioxane / H <sub>2</sub> O	1.2 / 1.7	75	65
7	Pyridine / H <sub>2</sub> O	1.2 / 1.7	29	10

Reaction conditions: Au (0.4 mol%), TiO<sub>2</sub> (P25), MAL (2 mmol), in 40 mL autoclave. <sup>a</sup> GC analyses.



The effect of solvent on the methacrolein oxidation reaction was investigated using 1wt%Au-1wt%Mg/TiO<sub>2</sub> as a catalyst. MAL conversion and MAA yield are shown in Table 3. During the aldehyde oxidation reaction, water can hydrate with the aldehyde to form a geminal diol [3.39]. However, a large amount of water may accelerate self-polymerization between unsaturated aldehydes [3.40]. Firstly, a mixed solvent (about 3 mL) of *t*-BuOH and water were investigated. The effect on the methacrolein oxidation reaction was observed while gradually increasing the amount of water from 0.4 mL. MAL conversions increased from 47% to 70% with increasing water, but MAA selectivity decreased slightly from 85% to 76%. Therefore, the optimal ratio of mixed solvent (*t*-BuOH/H<sub>2</sub>O) is 1.2 / 1.7. Secondly, three organic solvents (heptane, 1,4-dioxane, pyridine) with boiling points of about 100°C were examined. Same as *t*-BuOH, for both heptane and 1,4-dioxane which are non-polar solvents, even though more than 70% MAL conversion was obtained, the selectivity of MAA was always kept at about 60%. In the case of pyridine which is a polar aprotic solvent, the methacrolein oxidation reaction was hard to conduct and the MAL conversion was less than 30%. Therefore, it was concluded that the optimal solvent was *t*-BuOH: H<sub>2</sub>O = 1.2: 1.7 among the investigated solvents.

### 3.3.1.4 Examination of Transition Metals as Secondary Metals

**Table 4.** Effect of Addition of transition metals as second metal was investigated.

$$\text{MAL} \xrightarrow[\text{Air, 4 h}]{\text{Au-M/TiO}_2, \text{ } t\text{-BuOH/H}_2\text{O}} \text{MAA}$$

Entry	catalyst <sup>a</sup>	Conv. (%) <sup>b</sup>	Selec. (%)
1	1wt%Au-0.6wt%Mn/TiO <sub>2</sub>	82	79
2	1wt%Au-2.8wt%Re/TiO <sub>2</sub>	45	71
3	1wt%Au-1wt%Zn/TiO <sub>2</sub>	68	79
4	1wt%Au-0.9wt%Ni/TiO <sub>2</sub>	64	83
5	1wt%Au-0.9wt%Cu/TiO <sub>2</sub>	45	62
6	1wt%Au-0.8wt%Cr/TiO <sub>2</sub>	35	48
7	1wt%Au-1wt%Fe/TiO <sub>2</sub>	74	8
8	1wt%Au-2.1wt%La/TiO <sub>2</sub>	63	67
9	1wt%Au-2.1wt%Pr/TiO <sub>2</sub>	59	66

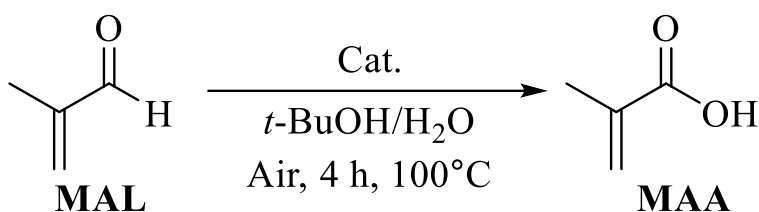
Reaction conditions: MAL (2 mmol), *t*-BuOH (1.2 mL), H<sub>2</sub>O (1.7 mL) and air (1.0 MPa) in 40 mL autoclave. <sup>a</sup> Atomic ratio about Au : M = 1 : 3. <sup>b</sup> GC analyses.

Furthermore, transition metal oxides were investigated as the second metals, the transition metals, MAL conversion and MAA selectivity were summarized in Table 4. All catalysts were prepared by the DP-IP method. The reaction promotion effect was observed when Mn, Zn, Ni and Pd oxides were added. In particular, the addition of Mn oxide gave the best results. In comparison with basic Mn oxide, acidic Re oxide which also belongs to group 7 was examined, but the MAL conversion (45%) was greatly reduced. In addition, when Cu, Cr, and Fe were added in Au/TiO<sub>2</sub> as the second metals, respectively, the reaction promotion effect was not observed.

With the addition of Fe, the MAL conversion was 74%, whereas the MAA selectivity was only 8%. However, no new by-products were found from the result based on gas chromatograph analysis, suggesting that MAL may be polymerized or decomposed to CO<sub>2</sub>. Finally, when the lanthanoid elements (La and Pr) were examined, there was no significant reaction promotion effect was observed. Therefore, the highest MAL conversion of 82% and MAA yield of 65% were obtained with the Mn-doped Au catalyst.

Table 5 shows the results of the active species for the reaction, the amount of loaded Mn, and the reaction temperature with the optimal Au-Mn/TiO<sub>2</sub> catalyst.

**Table 5.** Investigation of conditions for Mn as the second metal.



Entry	catalyst	Conv. (%) <sup>a</sup>	Selec. (%)
1	TiO <sub>2</sub>	19	21
2	0.6wt%Mn/TiO <sub>2</sub>	23	9
3	1wt%Au/TiO <sub>2</sub>	58	77
4	1wt%Au-0.2wt%Mn/TiO <sub>2</sub>	64	78
5	1wt%Au-0.4wt%Mn/TiO <sub>2</sub>	77	73
6	1wt%Au-0.6wt%Mn/TiO <sub>2</sub>	82	79
7	1wt%Au-0.8wt%Mn/TiO <sub>2</sub>	84	73
8	1wt%Au-1wt%Mn/TiO <sub>2</sub>	83	73
9	1wt%Au-2wt%Mn/TiO <sub>2</sub>	87	70
10	1wt%Au-4wt%Mn/TiO <sub>2</sub>	86	66
11	1wt%Au-12wt%Mn/TiO <sub>2</sub>	78	59
12 <sup>b</sup>	1wt%Au-0.6wt%Mn/TiO <sub>2</sub>	94	88

Reaction conditions: Au = 0.4 mol%, MAL (2 mmol), *t*-BuOH (1.2 mL), H<sub>2</sub>O (1.7 mL) and air (1.0 MPa) in 40 mL autoclave. <sup>a</sup> GC analyses. <sup>b</sup> Au = 1.2 mol%, 24 h, 50°C.

The conversion of MAL and selectivity of MAA with 0.6 wt% Mn/TiO<sub>2</sub> and TiO<sub>2</sub> were lower, which are 23%, 9% and 19%, 21%, respectively. As a result, these reactions hardly progressed (Entries 1, 2). On the other hand, 58% MAL conversion and 77% MAA selectivity were observed in 1 wt% Au/TiO<sub>2</sub> (Entry 3). Therefore, Au was definite to be the active species in the methacrolein oxidation reaction. For the reaction system with the load of Au (1 wt%) and Mn on TiO<sub>2</sub>. Under the condition of Mn ≤ 0.6wt%, the MAL conversion showed an increase from 64% to 82% (Entries 3–6) and the MAA selectivity kept stable. For the condition of 0.6wt% < Mn < 1wt%, there was no significant change

found in MAL conversion, but MAA selection decreased slightly from 79% to 73% (Entries 7, and 8). However, when Mn > 1 wt%, there was little change in MAL conversion which kept around 80%, but the MAA selectivity tended to decrease by 14% gradually (Entries 9–11). This is probably caused by that the reaction active sites of Au are covered by a large amount of loaded Mn.

However, the highest MAA selectivity was only about 80% with the optimal 1wt%Au-0.6wt%Mn/TiO<sub>2</sub> catalyst. This is probably caused by the polymerization of MAL and MAA which have a double bond structure. This could also be proved by the photos of the solution after the reaction (Figure 4). It is significant that MAL polymers (pale yellow) and MAA polymers (white) were produced. Therefore, the self-polymerization of the substrate MAL and the product MAA is considered to be one of the reasons for the decrease of MAA selectivity. Interestingly, 94% MAL conversion and 88% MAA selectivity (Table 5, Entry 12) were obtained with the increase of the amount of 1wt%Au-0.6wt%Mn/TiO<sub>2</sub> catalyst (Au = 1.2 mol%) under the 24h-reaction temperature of 50°C. In this condition, the self-polymerization of substrate MAL and the product MAA could be suppressed.

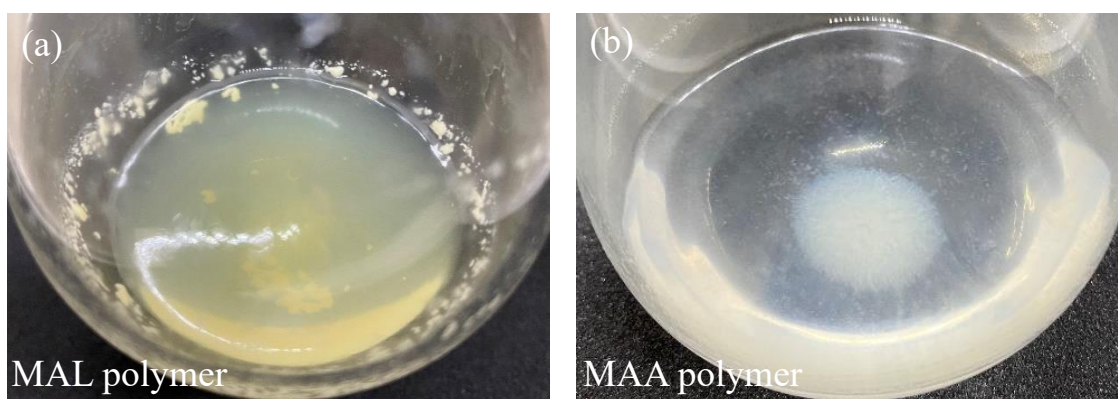


**Figure 4.** Photo of precipitated polymer (a) MAL polymer, (b) MAA polymer

### 3.3.2 Characterization of Catalyst

The reactant methacrolein mainly reacts on the surface of the Au catalyst. Catalyst characterization is a necessary analysis to understand the catalytic activity during the oxidation of methacrolein. Therefore, the accelerated reaction effects of Mn addition on MAL oxidation reaction based on Au-Mn/TiO<sub>2</sub> catalysts were investigated.

**Table 6.** Au, Mn loading and Particle size of Au measured by MP-AES and STEM in the as-prepared mono (Au or Mn) and bimetallic Au-Mn catalysts, respectively.

Catalysts	Addition amount of metal (wt%)				Experimental metal loadings (wt%) <sup>a</sup>				Particles size (nm)
	Au	Mn	Au/Mn	Au/Mn <sup>b</sup>	Au	Mn	Au/Mn	Au/Mn <sup>b</sup>	
1wt%Au/TiO <sub>2</sub>	1.2	ND	—	—	1.06	ND	—	—	3.1 ± 0.7
0.6wt%Mn/TiO <sub>2</sub>	ND <sup>c</sup>	0.6	—	—	ND	0.59	—	—	ND
1wt%Au-0.2wt%Mn/TiO <sub>2</sub>	1.2	0.2	6	1.68	1.10	0.16	6.88	1.92	2.9 ± 0.6
1wt%Au-0.4wt%Mn/TiO <sub>2</sub>	1.2	0.4	3	0.84	1.13	0.37	3.05	0.85	2.4 ± 0.5
1wt%Au-0.6wt%Mn/TiO <sub>2</sub>	1.2	0.6	2	0.56	1.01	0.62	1.63	0.45	2.3 ± 0.6
1wt%Au-0.8wt%Mn/TiO <sub>2</sub>	1.2	0.8	1.5	0.43	1.05	0.82	1.28	0.36	2.5 ± 0.7
1wt%Au-1wt%Mn/TiO <sub>2</sub>	1.2	1	1.2	0.34	1.07	1.12	0.96	0.29	2.4 ± 0.7

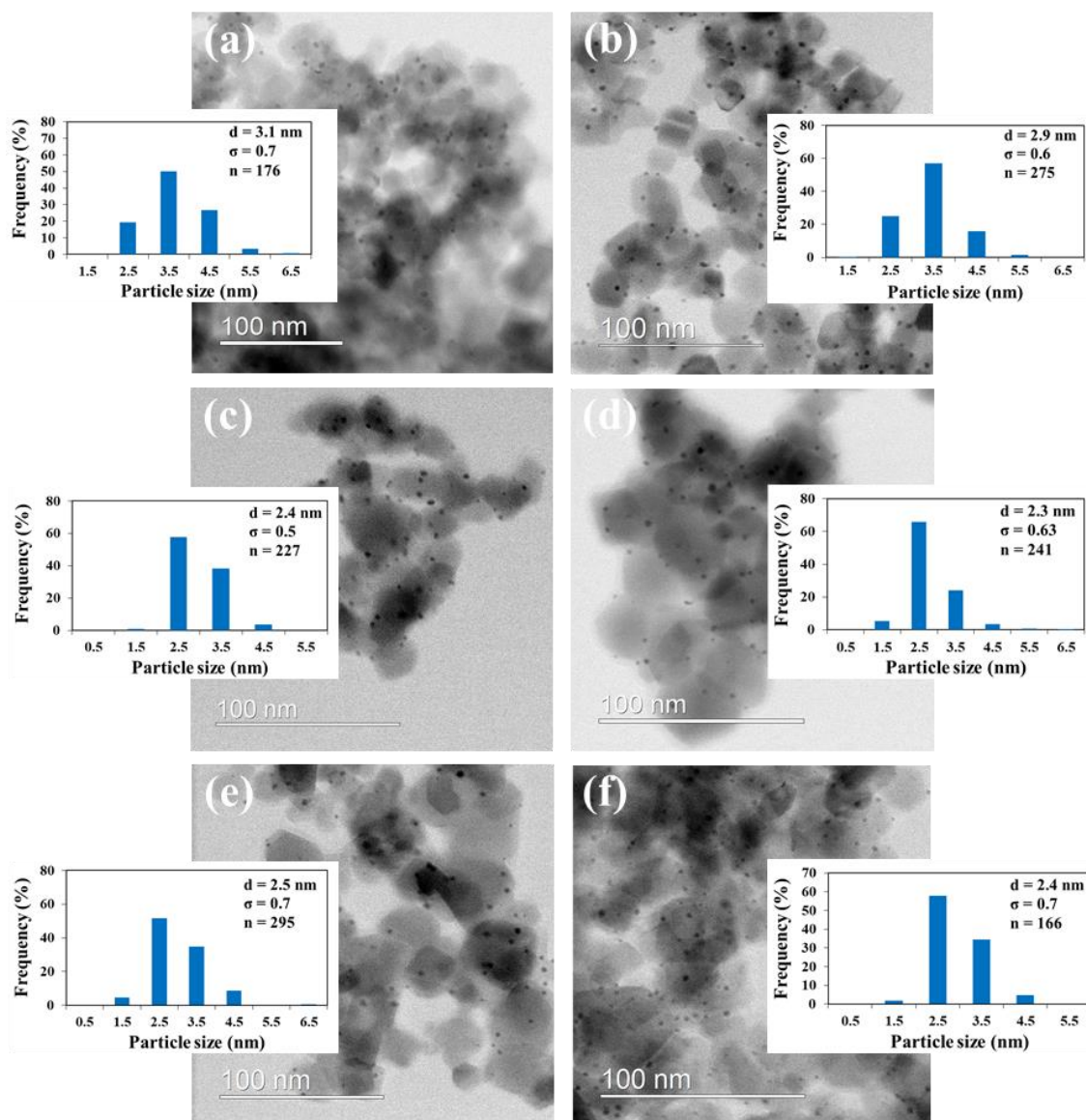
<sup>a</sup> MP-AES analyses. <sup>b</sup> Molar ratio. <sup>c</sup> Not detected. .

Table 6 shows the loaded amounts of Au and Mn and the molar ratio of Au/Mn measured by MP-AES. The Au loadings determined from MP-AES are always lower than added Au (Table 6). This could be caused by the preparation method in solution, which involves the deposition of Au and several post-preparation steps (filtration and washing). Mn was supported using the impregnation method. It is difficult to add Mn accurately since the precursor of Mn is a hydrate. However, the observed differences in the present study are quite reasonable and allow a comparison of the catalysts' series with various metal compositions.

It can be concluded from STEM images that Au nanoparticles prepared by DP were dispersed homogeneously on the TiO<sub>2</sub> support. Unfortunately, it was difficult to observe Mn nanoparticles in the catalyst prepared in the present study, since the Mn nanoparticles were too small to distinguish in the STEM images.

From the respective average particle sizes, it was clarified that the Au nanoparticles size of the bimetal-supported catalysts (2.3~ 2.9 nm) were smaller than those of the single metal-supported catalyst (3.1 nm). The decrease in Au nanoparticle size is considered to be related to the addition of Mn. The addition of Mn could affect the Au nanoparticle formation with different nucleation processes during the catalyst preparation [3.41].

## STEM Analysis



**Figure 5.** STEM-BF images and histograms of particle size of as-prepared Au-Mn/TiO<sub>2</sub> catalysts. (a) 1wt%Au/TiO<sub>2</sub>, (b) 1wt%Au-0.2wt%Mn/TiO<sub>2</sub>, (c) 1wt%Au-0.4wt%Mn/TiO<sub>2</sub>, (d) 1wt%Au-0.6wt%Mn/TiO<sub>2</sub>, (e) 1wt%Au-0.8wt%Mn/TiO<sub>2</sub>, (f) 1wt%Au-1wt%Mn/TiO<sub>2</sub>

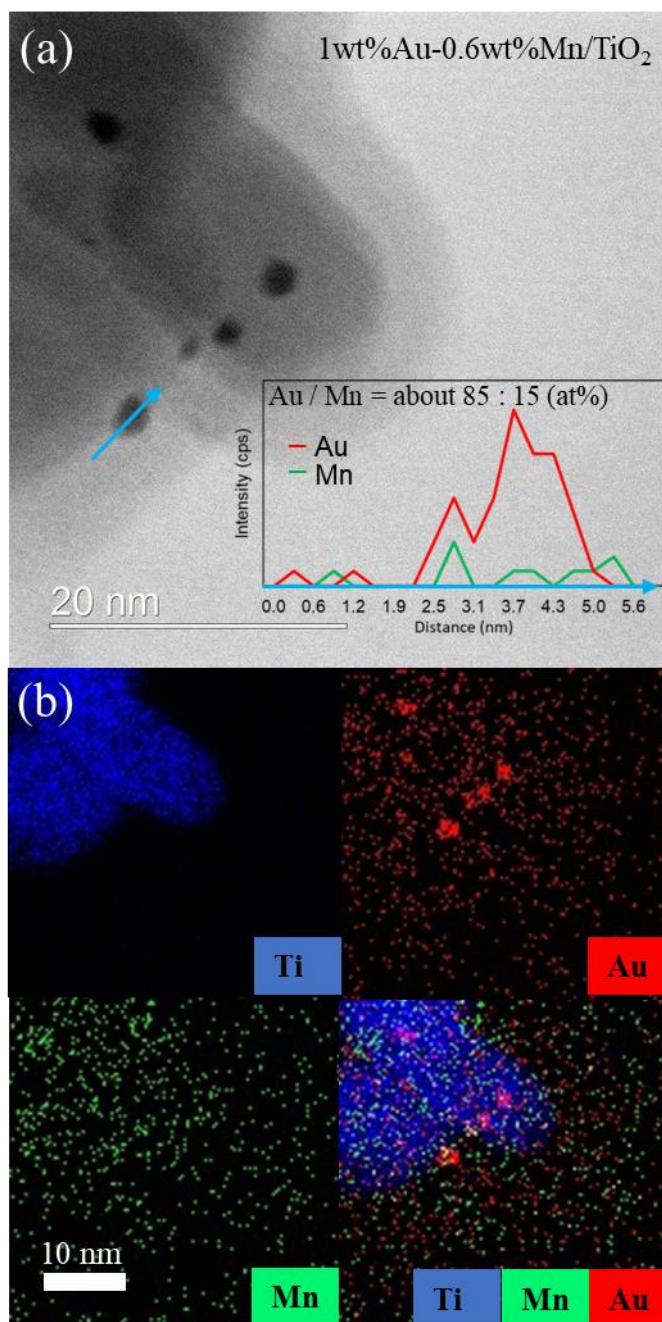


**Figure 6.** (a) STEM-BF image and (b) EDS mapping of 1wt%Au-0.6wt%Mn/TiO<sub>2</sub>

The 1wt%Au-0.6wt%Mn/TiO<sub>2</sub> catalyst was taken as an example for EDS mapping analysis to confirm the presence of Mn (Figure 6). Au and Mn particles are observed to be dispersed homogeneously on the surface of TiO<sub>2</sub>, and most of them are distant from each other (Figure 6b). However, it was confirmed by EDS mapping that a part of Mn is also present on the surface of Au. One of the Au particle (blue arrow in Figure 6a) was analyzed by line-scan (Figure 6b) and the atomic

percentages of Au and Mn was calculated as 85:15. This is considered a prerequisite for the interaction of the two metals.

### XRD Analysis

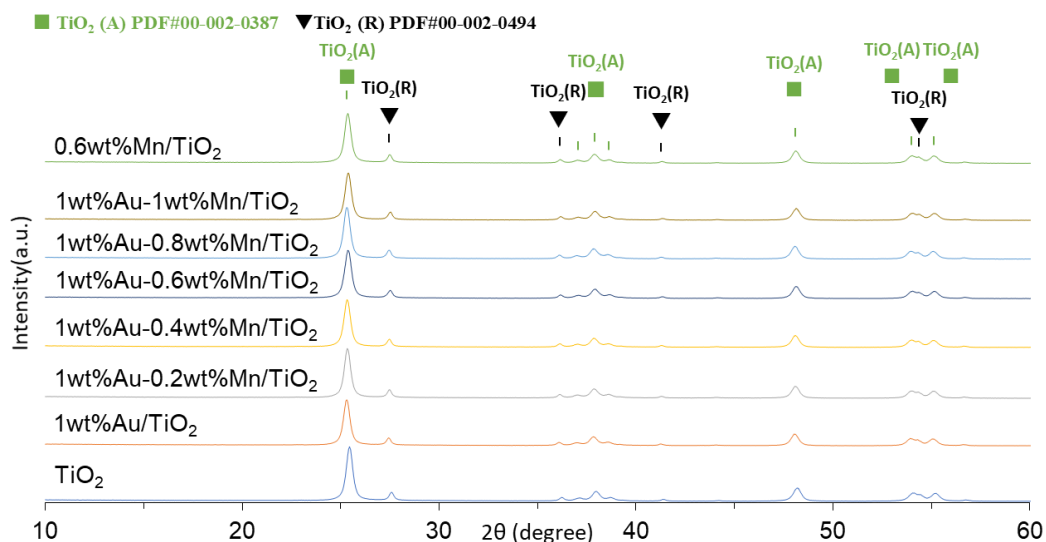


**Figure 7.** Powder XRD patterns for TiO<sub>2</sub>, as-prepared Au/TiO<sub>2</sub>, Mn/TiO<sub>2</sub> and Au-Mn/TiO<sub>2</sub> taken at room temperature.

All catalysts were examined by powder XRD and shown together with the TiO<sub>2</sub> support pattern for comparison. However, the XRD of all Au-Mn/TiO<sub>2</sub> supported catalysts was the same as that of the supported TiO<sub>2</sub> (Figure 7). As expected, two kinds of peaks (anatase PDF#00-002-0387, and rutile PDF#00-002-0494) derived from TiO<sub>2</sub> crystal structures were detected for all the catalysts. There was no impurity peak was observed in the XRD spectrum, illustrating the high purity of the samples. Besides, diffraction peaks related to the Mn was also not observed, which can be inferred to be low content (<5 wt%) or small metals (<5 nm) [3.42]. The typical Au diffraction peak of the plane (111) around 38.9° was not found indicating that Au nanoparticles were highly dispersed. This is also consistent with the result of STEM.



## XPS Analysis

Information about the oxidation states of Au, Mn, Ti and O on the catalyst surface (not detected by XRD) was obtained XPS. The identification of Au 4f, Mn 2p, Ti 2p and O 1s of all catalysts are shown in Figures 7, 8, 10, and 11. Different Au 4f and Mn 2p photoelectron peaks corresponding to surface Au and Mn species were found depending on the catalysts' formulation, and the results are listed in Table 7. It could be contributed by the binding energy variety from the interaction of both Au and Mn existing on the surface of Au.

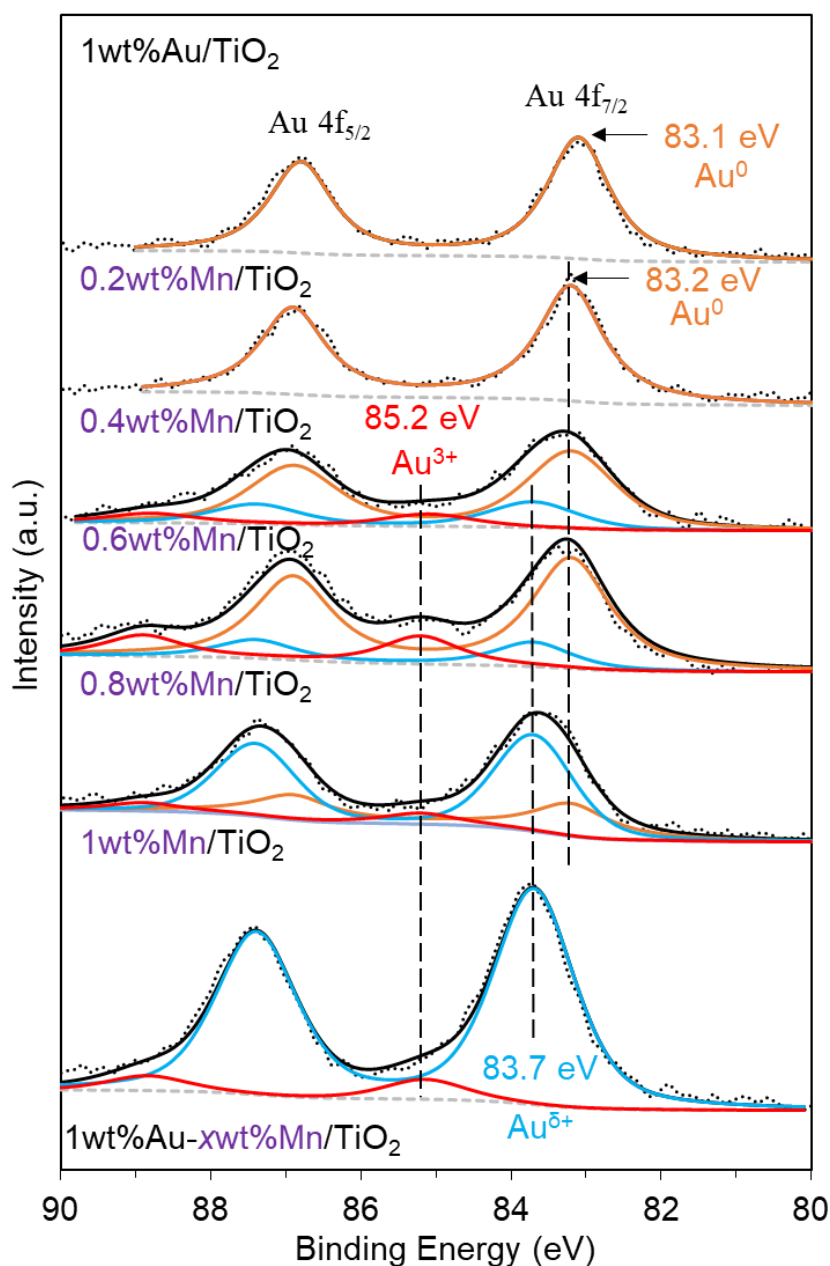


**Figure 7.** Au 4f XPS spectra of Au/TiO<sub>2</sub> and 1wt%Au-xwt%Mn/TiO<sub>2</sub> catalysts.

Au 4f XPS spectra of all Au-Mn/TiO<sub>2</sub> and 1wt% Au/TiO<sub>2</sub> catalysts were investigated (Figure 7, and Table 7). 1wt%Au/TiO<sub>2</sub> and 1wt%Au-0.2wt%Mn/TiO<sub>2</sub> have only one peak from metallic Au [3.43, 3.44], 1wt%Au-0.4wt%Mn/TiO<sub>2</sub>, 1wt%Au-0.6wt%Mn/TiO<sub>2</sub> and 1wt%Au-0.8wt%Mn /TiO<sub>2</sub> have three Au surface states (Au<sup>0</sup>, Au<sup>δ+</sup>, Au<sup>3+</sup>), and 1wt%Au-1wt%Mn/TiO<sub>2</sub> have two Au surface states (Au<sup>δ+</sup>, Au<sup>3+</sup>) [3.45, 3.46]. FWHM in all the figures was around 1.3 eV. Au-Mn/TiO<sub>2</sub> showed a binding energy positive shift by 0.1 eV compared to Au/TiO<sub>2</sub>, and most of the Au<sup>0</sup> metals became to Au<sup>δ+</sup> (about 91%) in 1wt%Au-1wt%Mn/TiO<sub>2</sub> catalyst (Table 7). It is possible that the interaction between Au and support has weakened with the addition of Mn. Moreover, the oxidized Au (Au<sup>3+</sup>) was observed in all of Au-Mn/TiO<sub>2</sub> catalysts except 1wt%Au-0.2wt%Mn/TiO<sub>2</sub>. In particular, the relative atomic ratio of oxidized Au (Au<sup>3+</sup>/Au = 17.1%) in 1wt%Au-0.6wt%/TiO<sub>2</sub> catalyst was the largest, whereas the other samples showed < 11% (Table 7). Although the reason for the formation of oxidized Au is still unclear, the addition of Mn may prevent Au from being fully reduced. It could be explained that the interaction between Mn and Ti existing nearby Au might change the interfacial electron distribution and might affect the electron transfer to Au. It was reported that oxygen vacancies occurred nearby Au that was supported on TiO<sub>2</sub> [3.47]. Besides, Li et al. calculated DFT, then reported that Mn could replace Ti or occupies oxygen vacancies in Ti<sub>2</sub>O<sub>3</sub> to form a stable Mn-Ti composite oxide [3.48]. Therefore, the additional agent of Mn as a secondary metal may affect the electron transfer to Au.

**Table 7.** The results of Au 4f (7/2) and Mn 2p (3/2) binding energy of catalysts and ratio of Au<sup>3+</sup> / Au and Mn<sup>4+</sup> / Mn.

Catalyst	Binding energy (eV)			Au <sup>3+</sup> / Au (%)	Binding energy (eV)			Mn <sup>4+</sup> / Mn (%)
	Au <sup>0</sup>	Au <sup>δ+</sup>	Au <sup>3+</sup>		Mn <sup>2+</sup>	Mn <sup>3+</sup>	Mn <sup>4+</sup>	
0.6wt%Mn/TiO <sub>2</sub>	-	-	-	-	640.5	642	644.1	16
1wt%Au/TiO <sub>2</sub>	83.1	0	0	0	-	-	-	-
1wt%Au-0.2wt%Mn /TiO <sub>2</sub>	83.2	83.7	0	0	640.5	642	644.1	28.4
1wt%Au-0.4wt%Mn /TiO <sub>2</sub>	83.2	83.7	85.2	10.8	640.5	642	644.1	26
1wt%Au-0.6wt%Mn /TiO <sub>2</sub>	83.2	83.7	85.2	17.1	640.5	642	644.1	36.6
1wt%Au-0.8wt%Mn /TiO <sub>2</sub>	83.2	83.7	85.2	9.5	640.5	642	644.1	19.6
1wt%Au-1wt%Mn /TiO <sub>2</sub>	0	83.7	85.2	8.7	640.5	642	644.1	17.9

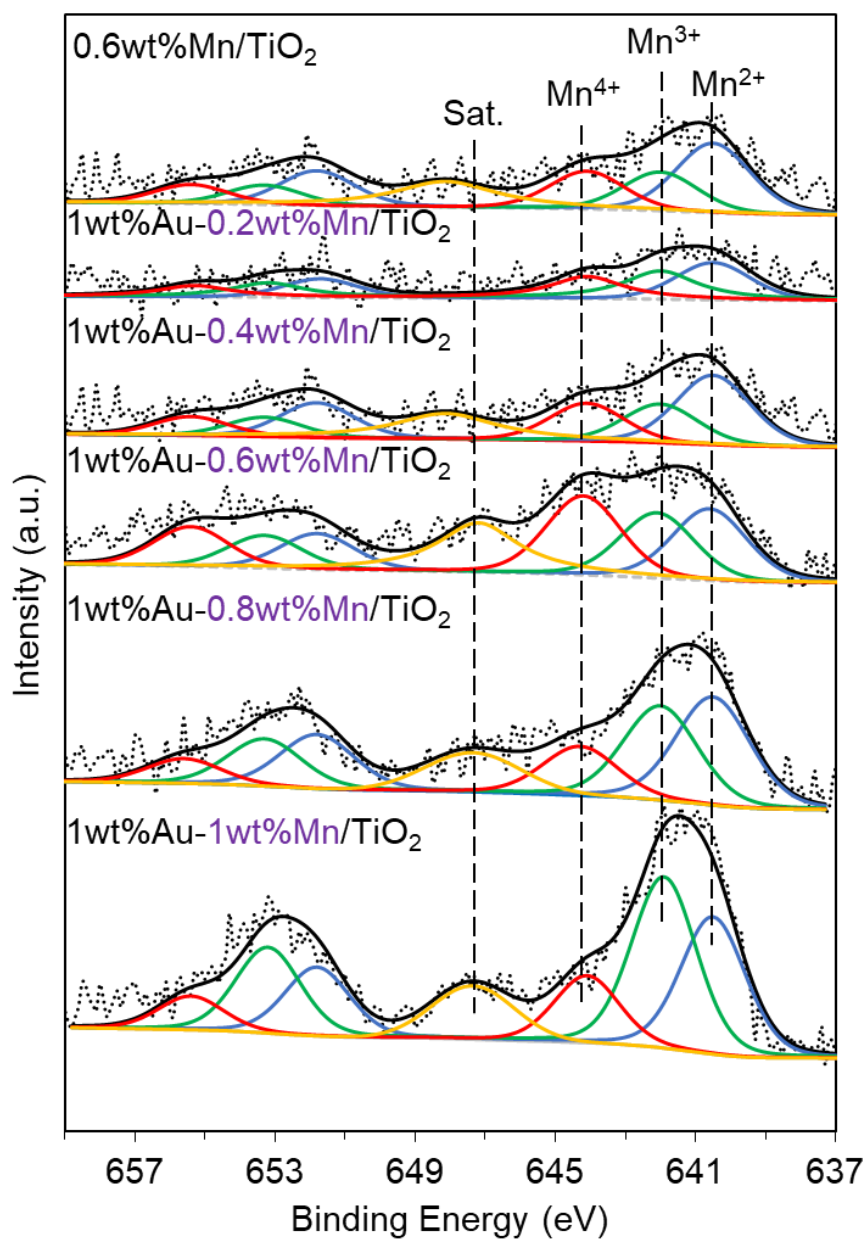


**Figure 8.** Mn 2p XPS spectra of Mn/TiO<sub>2</sub> and Au-Mn/TiO<sub>2</sub> catalysts.

Mn 2p XPS spectra for all Au-Mn/TiO<sub>2</sub> and 0.6wt% Mn/TiO<sub>2</sub> catalysts are shown in Figure 8, with two major peaks from Mn 2p<sub>3/2</sub> (640.5~ 644.1 eV) and Mn 2p<sub>1/2</sub> (651.8~ 655.4 eV). All samples were processed Based on 1wt%Au-1wt%Mn/TiO<sub>2</sub> which had a low noise effect, and three Mn surface states (Mn<sup>2+</sup>, Mn<sup>3+</sup>, and Mn<sup>4+</sup>) and satellite peaks were observed [3.49], respectively. The surface coverage of Mn (Mn<sup>4+</sup>) gradually increases with the amount of Mn, and the relative atomic ratio of Mn<sup>4+</sup> becomes a maximum of 36.6% in the case of 1wt%Au-0.6wt%Mn/TiO<sub>2</sub>.

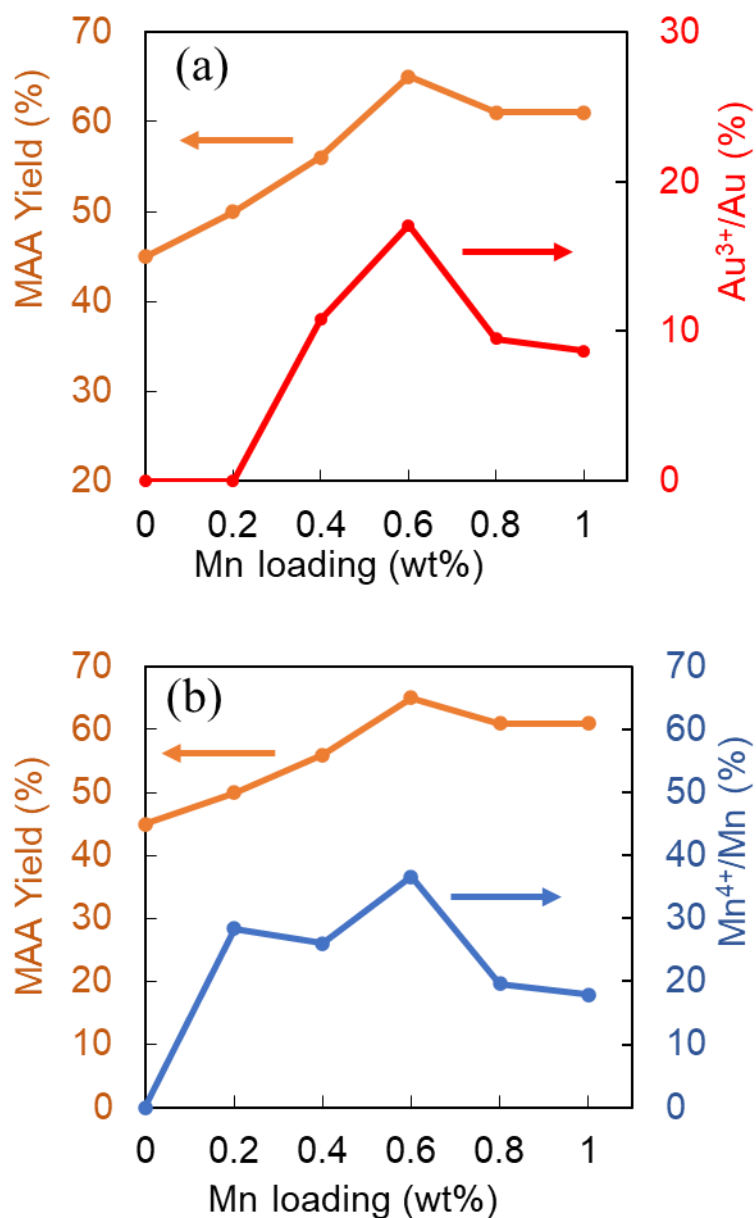


**Figure 9.** (a) Changes in MAA yield and ratio of  $\text{Au}^{3+}/\text{Au}$ , and (b) changes in MAA yield and ratio of  $\text{Mn}^{4+}/\text{Mn}$  for the catalysts of 1wt%Au- $x$ wt%Mn/ $\text{TiO}_2$ .

Interestingly, the ratio of  $\text{Au}^{3+}/\text{Au}$  and  $\text{Mn}^{4+}/\text{Mn}$  showed the same trend as the yield of methacrylic acid (Figure 9). When  $\text{Au}^{3+}$  was up to 17.1%, the ratio of  $\text{Mn}^{4+}$  on the catalyst surface was just up to 36.6%. Although Mn is not an active species, the addition of Mn may affect the amount of oxidized Au on the catalyst surface, which is one of the possibilities for accelerating the methacrolein oxidation reaction. However, although the amount of  $\text{Au}^{3+}$  decreased dramatically, the yield of MAA was still more than that of the catalyst with 1wt%Au/ $\text{TiO}_2$  because of the increased amount of  $\text{Au}^{\delta+}$ .

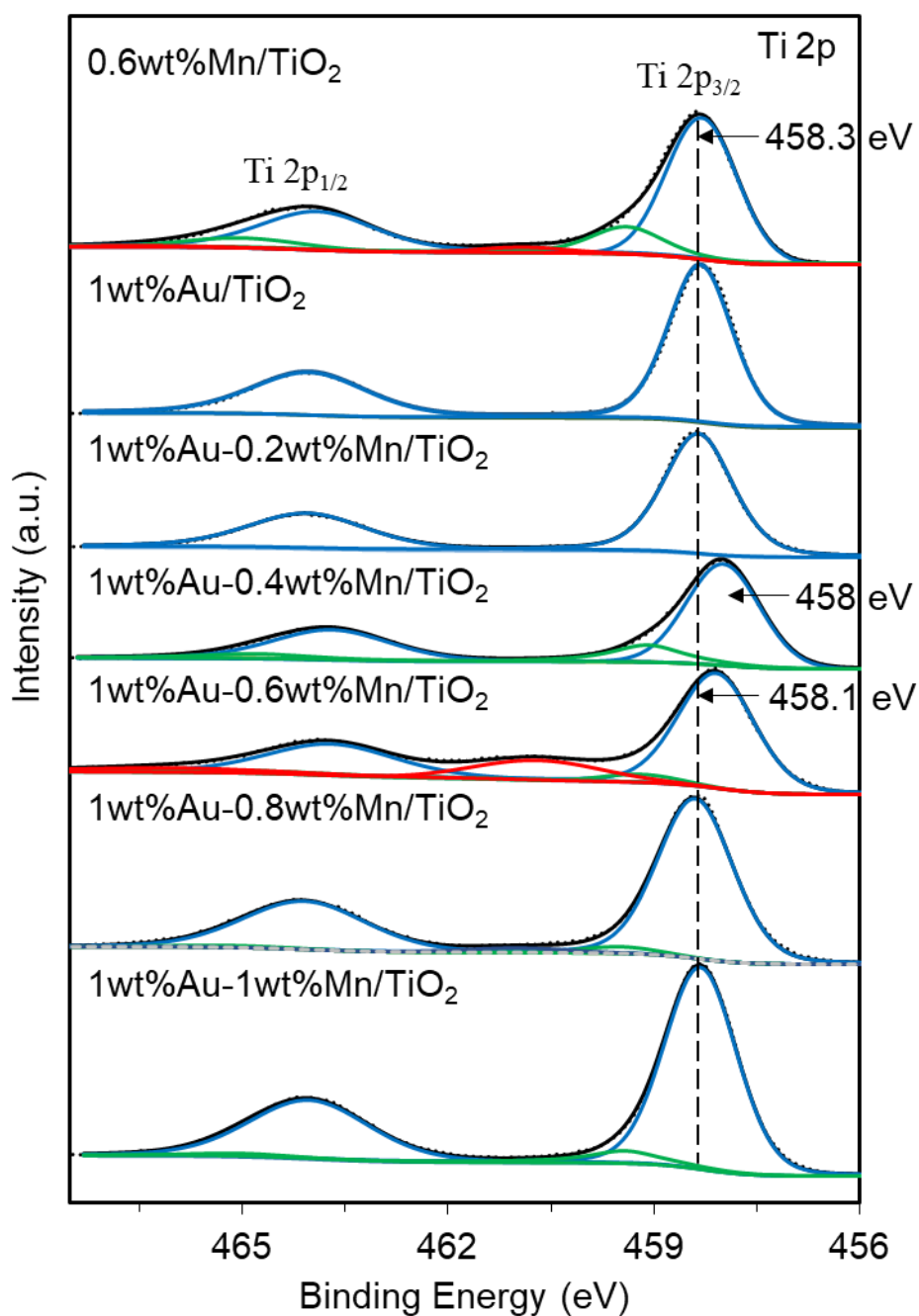


**Figure 10.** Ti 2p XPS spectra of Au/TiO<sub>2</sub>, Mn/TiO<sub>2</sub> and Au-Mn/TiO<sub>2</sub> catalysts.

XPS spectra of Ti 2p for all catalysts are shown in Figure 10. Two major peaks of Ti 2p<sub>3/2</sub> and Ti 2p<sub>1/2</sub> were found at 458-458.4 eV and 463.7-464.1 eV [3.54, 3.56], respectively. For 0.6wt%Mn/TiO<sub>2</sub>, two new peaks were observed at 459.4 and 460.9 eV, respectively. Although the exact phase of these peaks was still not clear, it was reasonable that they are related to the composite oxide composed by

titanium and manganese [3.50]. Moreover, the same phenomenon was also observed for the 1wt%Au-0.6wt%Mn/TiO<sub>2</sub> catalyst. Compared to 1wt%Au/TiO<sub>2</sub>, a negative shift of 0.3 and 0.4 eV was observed for 1wt%Au-0.4wt%Mn/TiO<sub>2</sub> and 1wt%Au-0.6wt%Mn/TiO<sub>2</sub>, respectively.

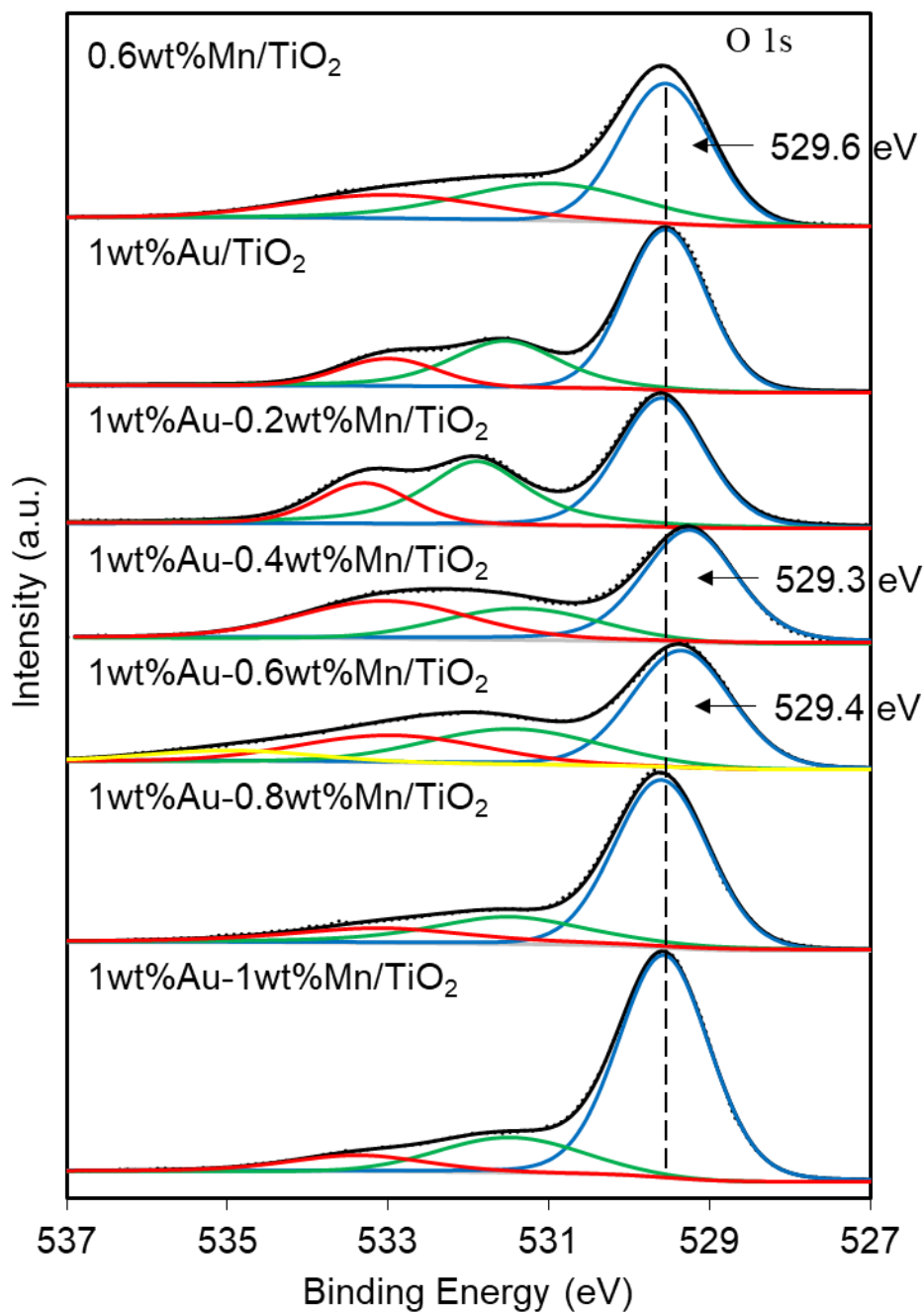


**Figure 11.** O 1s XPS spectra of Au/TiO<sub>2</sub>, Mn/TiO<sub>2</sub> and Au-Mn/TiO<sub>2</sub> catalysts.

The O 1s XPS spectra are shown in Figure 11. The first position (529.3–529.6 eV) corresponds to a large peak due to lattice oxygen in metal oxides. The second one (531–531.6 eV) is associated with oxygen species ( $O^-$ ,  $O^{2-}$ ,  $O_2^{2-}$  or OH) adsorbed on the catalyst surface. The third one (533–533.2) eV could be contributed to oxide from  $H_2O$  [3.44, 3.51]. In the case of 1wt%Au-0.6wt%Mn/TiO<sub>2</sub>, a small peak was detected on 535 eV, and which could be associated with organic carbon species. Notably, a significant negative shift by 0.2–0.3 eV for the O 1s can be observed when Mn = 0.4 and 0.6 wt%, compared with 1wt%Au/TiO<sub>2</sub> without Mn. Similarly, the negative shift by 0.2–0.3 eV was also observed for Ti 2p in the same catalysts (Figure 10). This could be caused by the electron migration from Au or Mn to TiO<sub>2</sub>, which could also lead to an increase in the proportion of Au<sup>3+</sup> and Mn<sup>4+</sup>.

### TPR analysis

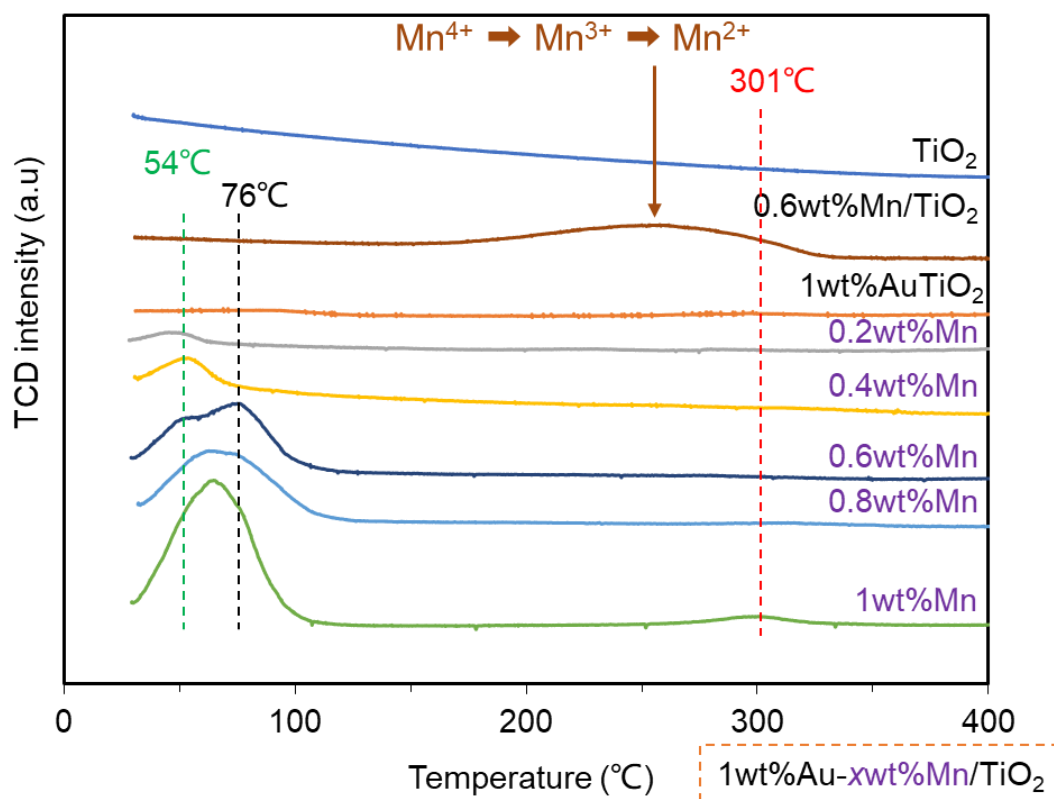


**Figure 12.** TPR spectra of TiO<sub>2</sub>, 0.6wt%Mn/TiO<sub>2</sub>, 1wt%Au/TiO<sub>2</sub> and various Au-Mn/TiO<sub>2</sub> catalysts.

The TPR spectra of P25 showed a poor reduction with H<sub>2</sub>, probably due to the presence of a large amount of the anatase phase of P25. The required energy of the oxygen vacancies in the different crystal phases of TiO<sub>2</sub>, as determined by DFT calculation, revealed that the rutile phase of TiO<sub>2</sub> on (110) required less energy to form oxygen vacancies than the anatase phase of TiO<sub>2</sub> on (001) [3.52]. However, the presence of mixed phases in the same unit volume might be more difficult to reduce.

When structures of TiO<sub>2</sub> with the maximum volume, the cell volume of TiO<sub>2</sub> (anatase) is 1.145 times as much to TiO<sub>2</sub> (rutile) [3.53]. The cell volume change might be increased the repulsion force of the same charge and thus affect the reducibility. Therefore, P25 showed an indistinguishable reduction peak in agreement with other reports [3.54]. For 0.6wt%Mn/TiO<sub>2</sub>, a wide reduction peak was observed in the range of approximately 200°C to 350°C. This might be caused by the reduction of MnO<sub>2</sub> to Mn<sub>2</sub>O<sub>3</sub> and Mn<sub>2</sub>O<sub>3</sub> to Mn<sub>3</sub>O<sub>4</sub> [3.55, 3.56]. Moreover, the wide range of the reduction peak might also contain Ti reduction peak [3.56]. For catalysts of 1wt%Au/TiO<sub>2</sub>, a weak reduction peak was observed around 500°C. This could be related to the reduction of Ti<sup>4+</sup> to Ti<sup>3+</sup> due to oxygen vacancies easily forming near the interface between Au and Ti. On the other side, a new reduction peak which could be associated with Mn was observed on the low-temperature side (<100°C) in the case of 1wt%Au-*x*wt%Mn/TiO<sub>2</sub> (0 < *x* < 0.4wt%) catalysts. It is possible that Au bound to the surface of TiO<sub>2</sub> could activate H<sub>2</sub>, making it more susceptible to dissociation. Using Au nanoparticles on anatase-type TiO<sub>2</sub> surfaces, Nie et al. investigated the effects of particle size and metal-support interactions by DFT calculation and adsorption, activation, and dissociation of H<sub>2</sub> through the structure of O<sup>2-</sup> – H<sup>+</sup> – H<sup>-</sup> – Au was reported [3.57]. Therefore, the dissociated H<sub>2</sub> could be facilitated the reduction of Mn and was reduced at the low-temperature. Furthermore, when 0.6 ≤ *x* ≤ 0.8wt%, two reduction peaks were observed on the low temperature side, the first peak (about 54°C) is the reduction peak of Mn<sup>4+</sup>, and the second peak (about 76°C) is likely the reduction peak from Mn<sup>3+</sup>. However, the reduction peak of Ti<sup>4+</sup> disappeared around 500°C. This suggests that the composite oxide of Mn and Ti makes Ti<sup>4+</sup> difficult to be reduced. It is also possible that Ti may be reduced together with Mn on the low-temperature side. Furthermore, a weak reduction peak was observed around 301°C in the case of *x* = 1wt%. It is probably related to the reduction of Mn<sup>3+</sup> to Mn<sup>2+</sup>.

### 3.4. Conclusions

Au was supported on various metal oxides (ZrO<sub>2</sub>, CeO<sub>2</sub>, TiO<sub>2</sub>, MgO, Al<sub>2</sub>O<sub>3</sub>, and NiO) by the DP method, and its effect on promoting the oxidation of methacrolein to methacrylic acid was investigated, and 1wt%Au/TiO<sub>2</sub> (P25) has the highest MAA selectivity (58%) in these catalysts. Besides, the oxidation reaction of methacrolein was also evaluated using a bimetallic catalyst (1wt%Au-*x*%M/TiO<sub>2</sub>, M = Mg, Ca, Ba, Re, Zn, Ni, Cu, Cr, Fe, La, and Pr, *x* = 0.6 ~ 2.8 wt%) which was prepared by the DP-IP method. As a result, 1wt%Au-0.6wt%Mn/TiO<sub>2</sub> catalyst showed a high MAL conversion (82%), and the MAA selectivity was 79% in the oxidation reaction of MAL. Furthermore, 88% MAA selectivity was obtained when the reaction temperature was lowered to 50°C. In contrast, the MAL conversion (about 20%) was also observed with the addition of 0.6wt%Mn/TiO<sub>2</sub> as low as that with TiO<sub>2</sub>, indicating that Au is the only active species.



For the catalysts of Au-Mn/TiO<sub>2</sub>, the factors promoting the oxidation of MAL were investigated by STEM, XPS and H<sub>2</sub>-TPR. As a result, the presence of oxidized Au might facilitate the oxidation reaction of MAL. In particular, more oxidized Au and Mn<sup>4+</sup> (Table 7) were observed for 1wt%Au-0.6wt%Mn/TiO<sub>2</sub> with high activity in the MAL oxidation reaction.

Finally, hopefully, our approach furthers the development of the oxidation reaction of methacrolein.

### 3.5. Reference

- 3.1 Darabi Mahboub, M. J.; Dubois, J.L.; Cavani, F.; Rostamizadeh, M.; Patience, G. S. *Chem. Soc. Rev.* **2018**, *47*, 7703.
- 3.2 Zhou, L.; Wang, L.; Zhang, S.; Yan, R.; Diao, Y. *J. Catal.* **2015**, *329*, 431.
- 3.3 Liu, Y.; Wang, S.; Li, Y.; Gai, X.; Zhu, M.; Han, X. *Appl. Catal. A-Gen.* **2022**, *643*, 118789.
- 3.4 Zhou, L.; Wang, L.; Diao, Y.; Yan, R.; Zhang, S. *Mol. Catal.* **2017**, *433*, 153.
- 3.5 Wang, B.; Dong, H.; Lu, L.; Liu, H.; Zhang, Z.; Zhu, J. *Catalysts* **2021**, *11*, 394.
- 3.6 Ninomiya, W. *Catalysts & Catalysis* **2014**, *56*, 360.
- 3.7 Ninomiya, W. *Catalysts & Catalysis* **2020**, *62*, 106.
- 3.8 Frank, B.; Blume, R.; Rinaldi, A.; Trunschke, A.; Schlögl, R. *Angew. Chem. Int. Ed.* **2011**, *50*, 10226.
- 3.9 Zhou, L.; Sun, Y.; Li, B.; Li, Z.; Zhang, Z.; Yun, J.; Liu, R. *Catal. Commun.* **2019**, *126*, 44.
- 3.10 Shi, D. P.; Ji, H. B. *Chin. Chem. Lett.* **2009**, *20*, 139.
- 3.11 Biella, S.; Prati, L.; Rossi, M. *J. Mol. Catal. A Chem.* **2003**, *197*, 207.
- 3.12 Yu, H.; Ru, S.; Dai, G.; Zhai, Y.; Lin, H.; Han, S.; Wei, Y. *Angew. Chem. Int. Ed.* **2017**, *56*, 3867.
- 3.13 Sancineto, L.; Tidei, C.; Bagnoli, L.; Marini, F.; Lenardão, E. J.; Santi, C. *Molecules* **2015**, *20*, 10496.
- 3.14 Ninomiya, W.; Takeda, A.; Kawato, S. *Jpn. Kokai Tokkyo Koho (2004)*, publication No. JP 2004-141863.
- 3.15 Akihara, H.; Takeda, A.; Ninomiya, W. *Jpn. Kokai Tokkyo Koho (2012)*, publication No. JP 2012-176399.
- 3.16 Takenaka, A.; Akihara, H.; Takeda, A. *Jpn. Kokai Tokkyo Koho (2013)*, publication No. JP 2013-215671.
- 3.17 Hui, Y.; Zhang, S.; Wang, W. *Adv. Synth. Catal.* **2019**, *361*, 2215.

- 3.18 Tosoni, S.; Pacchioni, G. *ChemCatChem* **2019**, *11*, 73.
- 3.19 Ishida, T.; Koga, H.; Okumura, M.; Haruta, M. *Chem. Rec.* **2016**, *16*, 2278.
- 3.20 Nuhu, A.; Soares, J.; Gonzalez-Herrera, M.; Watts, A.; Hussein, G.; Bowker, M. *Top. Catal.* **2007**, *44*, 293.
- 3.21 Yang, X.; Wang, X.; Liang, C.; Su, W.; Wang, C.; Feng, Z.; Li, C.; Qiu, J. *Catal. Commun.* **2008**, *9*, 2278.
- 3.22 Abad, A.; Concepción, P.; Corma, A.; García, H. *Angew. Chem. Int. Ed.* **2005**, *44*, 4066.
- 3.23 Hong, Y.C.; Sun, K.Q.; Han, K.H.; Liu, G.; Xu, B.Q. *Catal. Today* **2010**, *158*, 415.
- 3.24 Wang, Z.; Xu, C.; Wang, H. *Catal. Lett.* **2014**, *144*, 1919.
- 3.25 Huang, R.; Fu, Y.; Zeng, W.; Zhang, L.; Wang, D. *J. Organomet. Chem.* **2017**, *851*, 46.
- 3.26 Grunwaldt, J.D.; Maciejewski, M.; Becker, O. S.; Fabrizioli, P.; Baiker, A. *J. Catal.* **1999**, *186*, 458.
- 3.27 Grzelczak, M.; Pérez-Juste, J.; Mulvaney, P.; Liz-Marzán, L. M. *Chem. Soc. Rev.* **2008**, *37*, 1783.
- 3.28 Luo, Z.; Zhao, G.; Pan, H.; Sun, W. *Adv. Energy Mater.* **2022**, *12*, 2201395.
- 3.29 Tihiro I.; Suzuki, K. *Jpn. Kokai Tokkyo Koho (2011)*, publication No. JP 2011-102253.
- 3.30 Zhang, L.; Paul, S.; Dumeignil, F.; Katryniok, B. *Catalysts* **2021**, *11*, 769.
- 3.31 Galzada, L. A.; Collins, S. E.; Han, C. W.; Ortalan, V.; Zanella, R. *Appl. Catal. B* **2017**, *207*, 79.
- 3.32 Kotolevich, Y.; Kolobova, E.; Mamontov, G.; Khramov, E.; Cabrera Ortega, J.E.; Tiznado, H.; Fariás, M.H.; Bogdanchikova, N.; Zubavichus, Ya.; Mota-Morales, J.D. Corberán Cortés, V.; Zanella, R.; Pestryakov, A. *Catal. Today* **2016**, *278*, 104.
- 3.33 Prati, L.; Villa, A.; Jouve, A.; Beck, A.; Evangelisti, C.; Savara, A. *J. Name.*, 2018,
- 3.34 Zhang, X.; Wang, H.; Xu, B.Q. *J. Phys. Chem. B* **2005**, *109*, 9678.
- 3.35 Hong, Y.C.; Sun, K.Q.; Han, K.H.; Liu, G.; Xu, B.Q. *Catal. Today* **2010**, *158*, 415.
- 3.36 Bu, Y.; Chen, Y.; Jiang, G.; Hou, X.; Li, S.; Zhang, Z. *Appl. Catal. B* **2020**, *260*, 118138.
- 3.37 Zope, B. N.; Hibbitts, D. D.; Neurock, M.; Davis, R. J. *Science* **2010**, *330*, 74.
- 3.38 Davis, S. E.; Zope, B. N.; Davis, R. J. *Green Chem.* **2012**, *14*, 143.
- 3.39 An, G.; Ahn, H.; De Castro, K. A.; Rhee, H. *Synthesis* **2010**, *3*, 477.
- 3.40 Henglein, V. A.; Schnabel, W.; Schuiz, R. C. A. HENGLEIN, *Angew. Chem.* **1959**, *71*, 181.

- 3.41 Wu, M.L.; Chen, D.H.; Huang, T.C. *Langmuir* **2001**, *17*, 3877.
- 3.42 Schade, O. R.; Kalz, K. F.; Neukum, D.; Kleist, W.; Grunwaldt, J.D. *Green Chem.* **2018**, *20*, 3530.
- 3.43 Sha, J.; Paul, S.; Dumeignil, F.; Wojcieszak, R. *RSC Adv.* **2019**, *9*, 29888.
- 3.44 Portillo-Vélez, N.S.; Zanella, R. *Chem. Eng. Sci.* **2020**, *385*, 123848.
- 3.45 Ye, J.; Zhu, B.; Cheng, B.; Jiang, C.; Wageh, S.; Al-Ghamdi, A. A.; Yu, J. *Adv. Funct. Mater.* **2022**, *32*, 2110423.
- 3.46 Chang, L.-H.; Sasirekha, N.; Chen, Y.-W. *Catal. Commun.* **2007**, *8*, 1702.
- 3.47 Widmann, D.; Krautsieder, A.; Walter, P.; Brückner, A.; Behm, R. J. *ACS Catal.* **2016**, *6*, 5005.
- 3.48 Hou, Y.; Zheng, W.; Wu, Z.; Li, G.; Moelans, N.; Guo, M.; Khan, B. S. *Acta Mater.* **2016**, *118*, 8.
- 3.49 Camposeco, R.; Castillo, S.; Nava, N.; Maturano, V.; Zanella, R. *Catal. Letters* **2020**, *150*, 3342.
- 3.50 Wu, Z.; Jiang, B.; Liu, Y. *Appl. Catal. B* **2008**, *79*, 347.
- 3.51 Meng, L.; Yang, T.; Yun, S.; Li, C. *Chin. Phys. B* **2018**, *27*, 016802.
- 3.52 Bouzoubaa, A.; Markovits, A.; Calatayud, M.; Minot, C. *Surf. Sci.* **2005**, *583*, 107.
- 3.53 Hu, H.; Lin, Y.; Hu, Y. H. *Phys. Lett. A* **2019**, *383*, 2978.
- 3.54 Eaimsumang, S.; Prataksanon, P.; Pongstabodee, S.; Luengnaruemitchai, A. *Res. Chem. Intermed.* **2019**.
- 3.55 Xie, J.; Yan, N.; Yang, S.; Qu, Z.; Chen, W.; Zhang, W.; Li, K.; Liu, P.; Jia, J. *Res. Chem. Intermed* **2012** *38* 2511.
- 3.56 Ettireddy, P. R.; Ettireddy, N.; Mamedov, S.; Boolchand, P.; Smirniotis, P. G. *Appl. Catal. B* **2007**, *76*, 123.
- 3.57 Wan, W.; Nie, X.; Janik, M. J.; Song, C.; Guo, X. *J. Phys. Chem. C* **2018**, *122*, 17895.

## **Acknowledgement**

At the completion of my graduation thesis, I wish to express my sincere appreciation to those who have offered me invaluable encouragement and support during the five years of PH.D. study in Kyushu University.

Firstly, my foremost thanks go to my supervisor, Professor Makoto Tokunaga who has given me numerous important suggestions and valuable guidance with incomparable patience during the period of my PH.D. study. He maintains an efficient communication with me to ensure that I can complete my experiment and paper smoothly.

My heart-felt thanks also go to Associate Professor Haruno Murayama, and Assistant professor Eiji Yamamoto for their invaluable advice and excellent courses which have nurtured my passion for the research and brought lots of benefits to me. Then, I am indebted to her / him, not just for his supervisory aid but also for his encouragement, wisdom, and friendship over the last five years.

My sincere thanks are also extended to Professor Ryoichi Kuwano for providing deuterium gas and valuable discussions. Dr. Tadahiko Kubota is gratefully thanked for fruitful discussions on KIE and Arrhenius plot parts and the early stage of the research. Special thanks are given to Yukari Uchida, the administrative assistant, for her kind support of daily laboratory life.

I would like to express my deep gratitude to Takumi Hiasa, Hiroki Mita, Kazunari Motohashi of Murata Manufacturing Co., Ltd. and Yuki Kato, Wataru Ninomiya of Mitsubishi Chemical Corporation for giving us helpful opinions and providing reagents and materials.

I own many thanks to and all the members of Tokunaga group, the Laboratory of Catalysis Organic Chemistry, who have provided me a great deal of help and cooperation during these five years.

Particular thanks go to my parents. Only with their selfless support, concern and love, can I overcome

those difficulties and pursue my study till now. I would like to express the most heartfelt gratitude to my wife Sun Hanying. Their loving considerations and helps are the source of my strength.